ORIGINAL PAPER

Investigation of acoustic events during shear loading of layered rock bridge: particle flow code approach

Seyed Davoud Mohammadi[1] · **Rahim Mortezaei**[1] · **Vahab Sarfarazi**[2] · **Soheil Abharian**[3]

Abstract

This research investigates acoustic emission (AE) phenomena during shear failure of layered rock bridges under different normal stresses using experimental punch tests and numerical simulation. Firstly, particle flow code (PFC) was calibrated by UCS and Brazilian experimental test results and then the shear behavior of the numerical model was verified by experimental punch test outputs. Finally, acoustic phenomena during shear failure of layered rock bridges were discussed. Rectangular specimens were utilized, incorporating a combination of different layers. These layers included a pairing of soft and hard materials, as well as variations such as a two-layered model comprising hard gypsum and soft gypsum. Furthermore, three-layered models were examined, featuring a soft interlayer in one case and a hard interlayer in another. Additionally, a four-layered model was employed for the investigation. In each model, two vertical edge fissures were introduced, with fissure lengths set at 20, 40, and 60 mm. The angle between bedding layers and shear loading direction was 90°. The results indicate that cracks initiate at the notch tip and propagate vertically until they meet the upper boundary. The frequency of significant Acoustic hits is tied to factors like crack initiation and material properties. Increasing the number of layers in the specimen leads to more Acoustic hits. The sequence of Acoustic hits between major hits is influenced by parameters such as bedding number and material properties. This correlation is attributed to different gypsum types on the shear surface. The findings from numerical bedding models mirror those from physical samples.

Keywords Bedding rock · Shear test · Normal stress · Acoustic emission · PFC^{2D}

1 Introduction

Composite strata refer to a geological formation encountered during tunnel excavation that comprises multiple types of rock layers with distinct lithological characteristics and varying mechanical properties. These strata can be considered as a combination of different rock formations in terms of their composition and behavior when tunneling through them. The mechanical behavior of a layered rock can be approximated as exhibiting transverse isotropy. This means that the shear behavior of the layered rock is influenced by factors such as

✉ Seyed Davoud Mohammadi
  d.mohammadi@basu.ac.ir

1 Department of Geology, Bu-Ali Sina University, Hamedan, Iran

2 Department of Mining Engineering, Hamedan University of Technology, Hamedan, Iran

3 Department of Civil and Environmental Engineering, Western University, London, ON, Canada
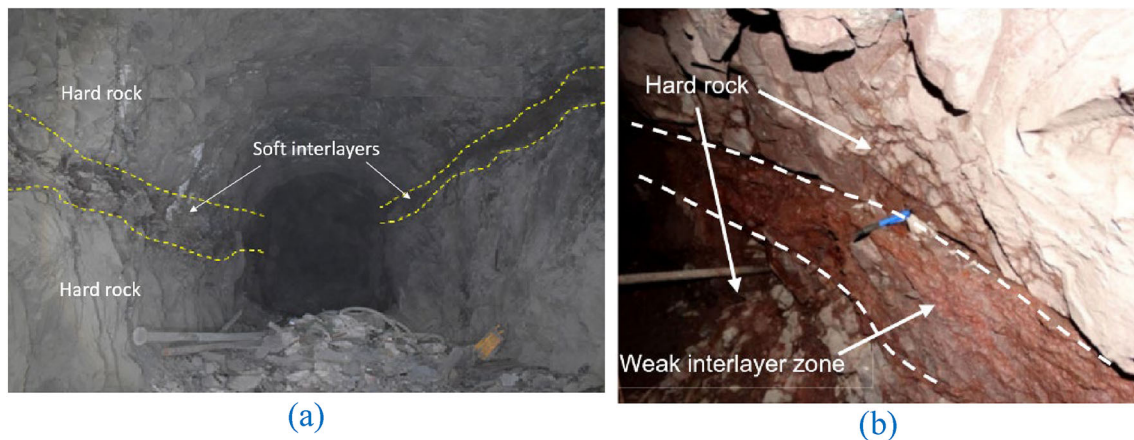
the mechanical properties of each individual layer, the layer's orientation, and the interaction at the interfaces between the layers. Consequently, the failure mechanism of the layered rock in this scenario can differ from that of a homogeneous and isotropic rock mass. In the study used by Xiao and Qiu (1983), a set of layered composite rock specimens has been created, consisting of sandstone, mudstone, and limestone. The researchers examined the impact of interface cohesion by splicing the layered composite rock specimens together using adhesives (Xiao and Qiu 1983). Numerous studies have created rock samples with transverse isotropy by using materials that resemble rocks. Tien et al. (2006) and Tien and Tsao (2000) was introduced a technique to produce layered blocks composed of cement and kaolin. Zhang et al. (2011, 2012) transverse isotropic rock specimens were prepared using a technique similar to Tien's method. These endeavors represent effective efforts to explore the shear failure mechanism of layered rock specimens. Wasantha et al. (2015) delved into exploring the impact of joint geometrical properties on the fracture characteristics of rock formations featuring joints.

Fig. 1 Hard rock with weak interlayer **a** weak interlayer in tunnel walls, **b** weak interlayer in vicinity of tunnel roof

In a parallel vein, Xiong et al. (2018) conducted experiments involving the preparation of layered rock samples to scrutinize their mechanical attributes when subjected to uniaxial compression. These studies suggest that the layer interfaces is considered as a joint sliding surface. Nasseri et al. (1997, 2003) were subjected schist samples to various tests, and a novel criterion was introduced to estimate both the modulus and strength of the material. Masri et al. (2014) and Niandou et al. (1997) and examined the characteristics of layered rock to understand its anisotropic properties. Hakala et al. (2007) studied the influences of axial compression load and indirect tensile stress on the mechanical properties of layered rock samples. Cho et al. (2012) experimentally investigate the deformation anisotropy of three distinct types of layered rock samples. The strength anisotropy and failure behavior of bedded sandstone were examined in a comprehensive investigation Wasantha et al. (2014). In this study, the influence of layered angel on the wave velocity along the layered amphibolite rock were measured, too. The aim was to explore the strength anisotropy of the specimens (Fig. 1).

Esamaldeen et al. (2014) and Gholami and Rasouli (2014) performed various mechanical tests on layered rock samples in order to examine the anisotropy of rock strengths. Yin and Yang (2018) examined the mechanical behavior of bedded sandstone by conducting both UCS test and indirect tensile test. The focus of their study was on investigating the anisotropy of mechanical behavior the layered rock. Yang et al. (2019a, b, 2020) conducted research on the damage anisotropy in layered rock. They employed X-ray imaging techniques to analyze the samples after performing triaxial tests. Chu et al. (2013), Park and Min (2012, 2015), Zhang et al. (2018), and Xiong et al. (2019), conducted discrete element simulations on specimens with transverse isotropy or jointed configurations. Their findings demonstrated strong concurrence with experimental studies. Jaeger (1960) render a theory to introduced two fracture patterns in layered

rock i.e. failure through the intact layered and failure along a layer interface. Then, Donath (1961) and Hoek and Brown (1980) made modifications to theory of Jaeger. Different fracture criteria have been proposed for layered rock such as Duveau and Shao (1998), Park and Min (2013), Duveau et al. (2015), Tien and Kuo (2001), Singh et al. (2015), Shi et al. (2016), Wang et al. (2016a, b) and Yin and Yang (2019). These researchers have put forth various criteria to assess failure in anisotropic materials. Theoretical predictions have exhibited strong agreement with experimental investigations in this area. Numerous scholars have conducted studies on the acoustic event properties observed during failure processes of layered rock in different types of tests. These investigations aim to scrutinize the mode of cracking under diverse mechanical tests. Lockner (1993) employed acoustic emission technology to investigate the complete deformation behaviour of rock specimens under axial load testing conditions. The study revealed that the spatial distribution of pre-existing stresses in rocks can influence the location of fracture initiation. Dang, et al. (2016) investigate the Shear behavior of a plane joint under dynamic normal load. Wang et al. (2024) studied the Elastic–plastic criterion solution of deep roadway surrounding rock based on intermediate principal stress and Drucker–Prager criterion. Cai et al. (2007) examined the time of initial crack formation by scrutinizing the Acoustic hits occurring during the crack propagation in rock samples. Aggelis et al. (2012, 2013) proposed that shear tests generate acoustic event waveform signals with longer wavelengths compared to that occurred in tensile tests. This conclusion was drawn from laboratory testing results and observations of acoustic event properties. In their study, Yang et al. (2012) investigated the deformation behaviour, failure mechanism, strength behavior, and acoustic emission phenomena of sandstone under triaxial test. The findings of their research indicated that the acoustic event hits generated due to shear crack development was more than that

generated by tensile crack propagation. Cheon et al. (2011) introduced an innovative monitoring device designed specifically for analyzing acoustic emission signals. This device was utilized to assess the damage in rock slopes by examining the changing ranges of acoustic emission count. Several researchers such as Chang and Lee (2004), Moradian et al. (2010), Liu et al. (2015), Zhao et al. (2013) and Abharian et al. (2022) have investigated the progressive evolution of rock fractures through the analysis of acoustic emission hits, acoustic emission energy characteristics, and acoustic event source positions. Tsuyoshi et al. (2010) demonstrated the effectiveness of acoustic emission technology in detecting crack propagation during direct shear testing of rocks. Their study confirmed that acoustic event technology exhibits high precision and sensitivity in this regard. Tham et al. (2005) shows that marble and granite samples exhibit distinct fracture surfaces and acoustic emission properties during uniaxial tensile tests. Importantly, these observations were found to be strongly correlated with the lithology of the respective rocks. The advancements in acoustic emission imaging have significantly contributed to the comprehension of rock failure modes. These developments have provided valuable support in this field, as demonstrated by the works of Katsaga et al. (2007), Li and Einstein (2017), and Meglis et al. (1995). In their study, Wang and Liu et al. (2015) conducted a series of direct shear tests and bending tests on sandstone samples. The objective was to examine the variation of acoustic emission hits under different test conditions. The findings indicated that the acoustic emission energy associated with shear crack was notably higher compared to that of tensile crack. Hu et al. (2019) utilized an acoustic event detection apparatus to analyze acoustic event phenomena during laboratory rock tests. They successfully located the positions of micro-cracks within the specimens and determined that the failure process of rock burst was predominantly governed by tensile cracks. Ohno et al. (2010) introduced two classification methods based on the characteristic count of acoustic emission events to differentiate failure mode in reinforced concrete and ordinary concrete under hydraulic expansion tests and four-point bending tests. The study revealed that the crack mode typically transitions from tensile crack to shear crack as the concrete approaches' failure. Ohtsu (2010) utilized the acoustic event technique to detect crack evolution in concrete samples. The aforementioned research endeavors have contributed significantly to enhancing our understanding of the connection between crack evolution and acoustic event phenomena. Nevertheless, previous researches primarily concentrated on investigating the characteristics of acoustic emission in specific rock types under particular loading conditions. There remains a scarcity of systematic analyses regarding the influences of layered rock on acoustic event properties. In this paper, the mechanisms of shearing in horizontal hard and weak rock layers.
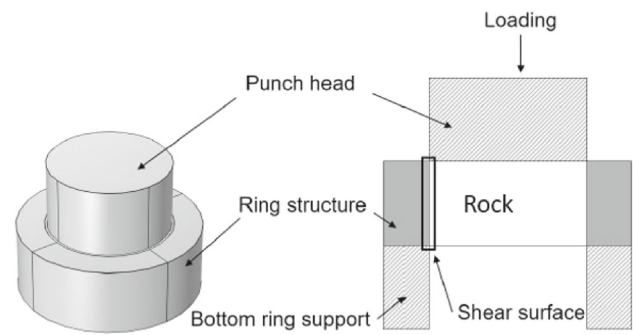

Fig. 2 Schematics of punch shear test setup and shear surface (Park et al. 2021)

The impact of factors such as the number of horizontal layers, thickness of the hard/weak bedding layers, brittleness of the layers, and normal stress have been studied on the acoustic event through shear testing. The study employed a three-step approach. First, PFC was calibrated via physical Brazilian tests and UCS tests. Second, the shear mechanism of layers resulting from PFC simulations and experimentally obtained ones were compared in the absence of normal stress. Finally, new PFC shear test was simulated to study the shear mechanism of bedding under a normal stress of 2 MPa.

2 Experimental section

2.1 Punch shear test

Punch shear test is the common test method to measure the shear strength of rock specimens. Shear stress is delivered by compressive force through a punch head and parallel to the shear surface (Zhu and Li 2021). The punch test illustrated in Fig. 2 consists of punch head, a rock sample, and bottom ring support. The punch head whose diameter is equal to the inner diameter of ring structure carries normal load to rock sample structure. Rock sample bears the compressive force on its shear surface where rock specimen meets ring structure, then is separated into rock specimen and ring structure if the shear stress exceeds rock shear strength. Bottom ring support props up only ring structure so that the rock specimen can be slipped alone. The shear strength τ could be calculated by Eq. (1) as a maximum value of the compressive force divided by the shear surface area (Park et al. 2021).

$$\tau = F_{max}/(\pi DH) \tag{1}$$

where F_{max} is a maximum value of compressive force, D is an inner diameter of ring structure, and H is a height of ring structure.

Table 1 Mixing ratio and mechanical properties of model material

Type	Ratio of gypsum/PVA/water	σ_c (MPa)	E (GPa)	σ_t (MPa)	σ_c/σ_t
Soft material	1/0/2	7.8	5.5	0.65	12
Hard material	1.3/0.043/2	12.2	8	1.55	7.8

2.2 Specimens preparation

In the conducted research, the preparation of samples involved a combination of polyvinyl acetate (PVA), gypsum, and water. Polyvinyl acetate, commonly recognized as wood/white/carpenters or PVA glue, constitutes a synthetic aliphatic rubbery polymer characterized by the chemical formula ($C_4H_6O_2$). The specific mixing ratios of model materials for both soft rock and hard rock were detailed in Table 1. Correspondingly, the mechanical properties of both soft rock and hard rock were obtained and are presented in the same table for reference. By combination of Polyvinyl acetate (PVA), gypsum, and water two type of material with different mechanical properties were prepared. The ratio of compressive strength to tensile strength for these two samples were 12 and 7.8, respectively (Table 1).

Various samples were created using a range of soft and hard layers in different combinations. These arrangements included: (a) A sample characterized by a sole soft layer is depicted in Fig. 3a. (b) Fig. 3b showcases a sample constructed with only a hard layer. Figure 3c shows a two-layered model comprising soft and hard material layers. Figure 3d depicts a three-layered model with a hard interlayer, while Fig. 3e presents a three-layered model with a soft interlayer. Finally, Fig. 3f illustrates a four-layered model consisting of two soft and two hard material layers.

All specimens were made to adhere to specific measurements: a width of 200 mm, a height of 240 mm, and a depth of 50 mm. whereas the height of UCT test machine chamber was 30 cm, therefor the height of samples was chosen to be equal to 24 cm. Also, by this dimension it's possible to create four layered with acceptable thickness (55 mm) within the sample.

Table 2 displays the thickness measurements for the soft material across various models, including the single soft layered, two-layered, three-layered with a hard interlayer, three-layered with a soft interlayer, and four-layered models. It's worth noting that in each model, the fissures were consistently sized at 20 mm in length and 1 mm in width.

2.3 Test equipment

The experiments on specimens containing parallel double fissure were conducted using UCS testing machine controlled by a microcomputer (refer to Fig. 3f). The machine has a

axial deformation measuring error of $\leq \pm 0.4\%$, a displacement control precision error of $\pm 0.2\%$, and a test force error of $\pm 0.2\%$. Axial and lateral control for displacement and force is provided, ensuring smooth transitions devoid of sudden impacts. In the experimental arrangement, a dual-purpose hydraulic jack with a load capacity of 225 tons and a stroke of 100 mm was utilized. Specimens were placed at the base center and subjected to loading at a controlled rate of 0.04 mm/min, managed through displacement regulation. Deformations were tracked using a linear variable differential transformer, while load and deformation measurements were recorded by a digital data logger throughout the experiments. Testing ceased when specimen load-bearing resistance dropped below 90% of the maximum applied load. Post-experiment, key parameters including shear displacement, failure patterns and shear force were meticulously recorded. Figures 4 and 5 present visual representations of crack development and the shear stress–shear displacement curve for a specific specimen named "PL 1.2" from the single hard-layered specimen group, respectively. From each layer configuration, three similar samples were prepared and tested by punch shear test (Fig. 3g).

Whereas one shear surface occur in notched sample due to presence of notches in only on side of sample therefore Eq. (1) should be rewritten as follow:
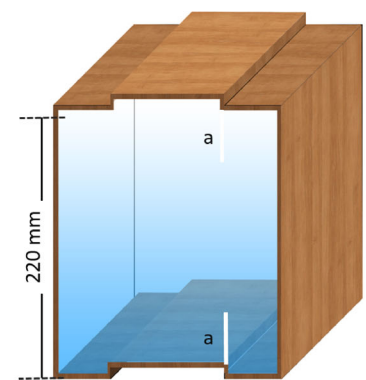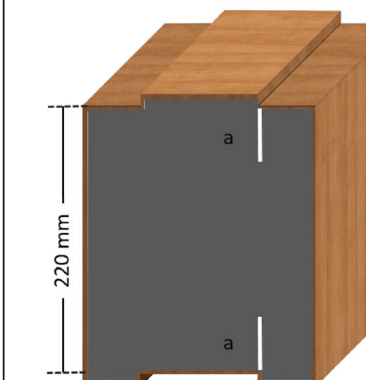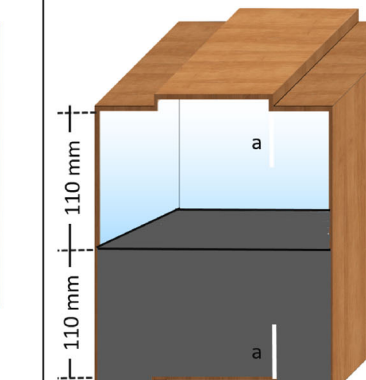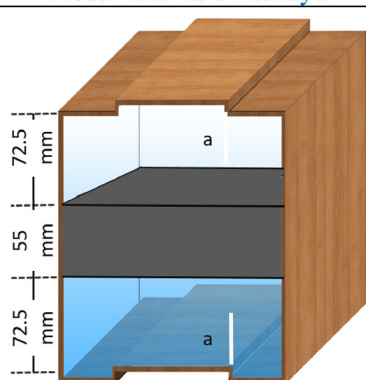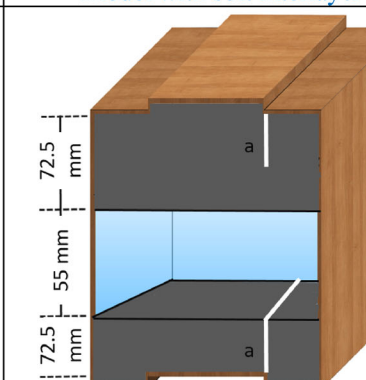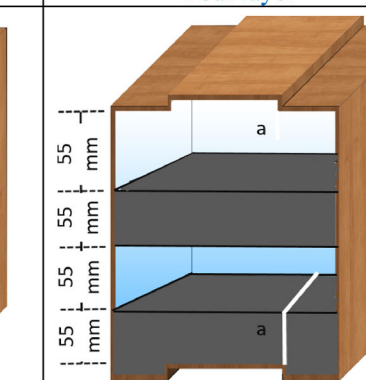
$$\tau = F_{max}/(5 \times 22) \qquad (2)$$

During the punch shear test (refer to Fig. 4), the specimen undergoes a transition from plasticity to elasticity and then back to plasticity, as indicated by the S-shaped curve. Under the continuous application of shear stress, the specimen's behavior changes throughout the test. During the loading phase, there is a stress drop resulting in energy loss. This energy loss is evident through the cracks initiation, propagation, and the crack coalescence. This phenomenon aligns with the Griffith theory proposed by Griffith (1921). Based on the fracture process and crack expansion in the specimen, we divided the shear stress-displacement curve of specimen PL 1.2 into three distinct stages: elastic stage (AB), crack initiation and slow propagation stage (BC), and rapid crack propagation and coalescence (CD).

Section AB represents the elastic deformation stage in Figs. 4a and 5. In this stage, although there are some irreversible deformations, such as the slight closure or opening of microscopic flaws, the primary deformation is elastic and

Fig. 3 Depict physical samples as follows: **a** a single soft layer, **b** a single hard layer, **c** a two-layered model, **d** a three-layered model with a hard interlayer, and **e** a three-layered model with a soft interlayer, **f** punch shear test device, **g** three similar samples tested from each layer configuration

Table 2 Ratio of thickness of material layers to total thickness of sample

follows Hoek's law (Hoek and Brown 1980). The shear stress applied to the specimen is linearly related to the corresponding shear displacement, resulting in an almost straight curve. Section BC corresponds to the stage of crack generation and slow propagation, as depicted in Fig. 4b–d. When the axial stress surpasses the resistance to crack propagation, the stress–strain curve exhibits nonlinearity, indicating plastic deformation. During this stage, more microstructures are damaged, and microcracks steadily expand. Simultaneously, the shear displacement increases at a reduced rate due to the generation and expansion of cracks. Point C on the curve signifies the stress yield limit, beyond which the fracture process progresses to the next stage. Section CD signifies the rapid crack growth stage, illustrated in Fig. 4e and f. This stage involves the appearance of macro-cracks over a significant area. When the shear stress exceeds the peak shear strength, it drops rapidly, while the axial strain undergoes minimal changes. At this point, the rock bridge is destroyed, resulting in a loss of its load-carrying capacity.

3 Numerical method

The particle flow code (PFC) incorporates numerical simulations using a flat-joint contact model (Fig. 6), which effectively represents the interface behavior between particles and rigid collections in hard rocks. This model allows for a larger ratio of uniaxial compressive strength (UCS) to tensile strength, typically ranging between 10 and 25.

The flat-joint model considers the interface between notional surfaces to be segmented into elements, which can be classified as either bonded or unbonded. Bonded elements demonstrate linear elastic characteristics, while unbonded elements exhibit both linear elastic and frictional behavior. Damage to the interface occurs when bonded elements break, resulting in partial damage. Additionally, the flat-joint model includes faced grains (spherical cores with skirted faces) to enhance grain interlocking and resist rotation after interface failure, resulting in a higher UCS to tensile strength ratio. Various numerical tests have been commonly used by researchers to determine UCS and tensile strength, such as the UCS test and the Brazilian test.
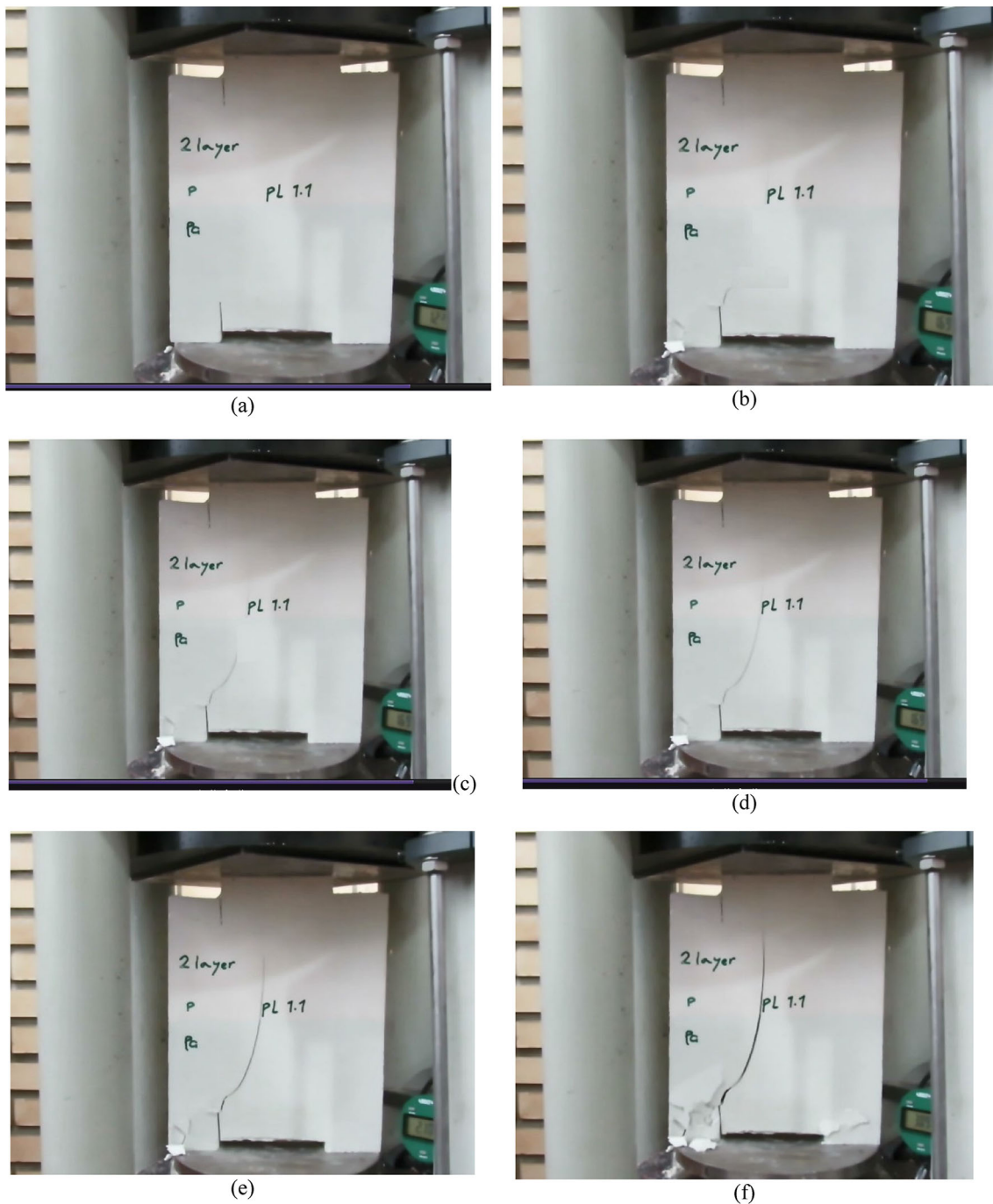
Fig. 4 Crack development during shear test

3.1 Determination micro parameter of numerical model

An essential aspect of the numerical tests involves calibrating the parameters of the flat-joint model. Several researchers (Li et al. 2018; Ren et al. 2018; Wu and Xu 2015) have introduced methods for parameter calibration. For model calibration, both of the UCS compressive strength and indirect Brazilian tensile strength should be calibrated. The primary approach used is numerical simulation, which allows for the adjustment of mechanical parameters such as compressive strength, Young's elastic modulus, and tensile strength to ensure their agreement with physical tests. The parameters for uniaxial compressive strength (UCS) and Young's elastic modulus are determined through numerical tests specifically designed for UCS, while the parameter for tensile strength
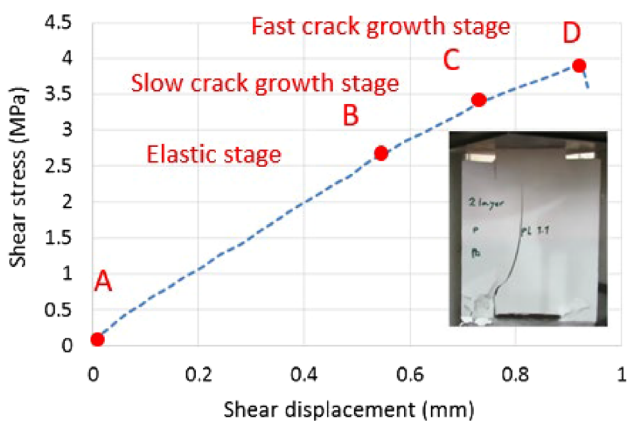
Fig. 5 Shear stress-displacement curve for single hard layer

is determined using Brazilian numerical tests. This calibration process ensures consistency between the model's parameters and the results obtained from physical experiments. The main micro parameters of the flat-jointed model are listed in Table 3. The mechanical properties of physical sample and numerical model were presented in Table 4. Table 5 presents a comparison between the failure patterns observed in experimental tests and the corresponding numerical results. The findings from this comparison highlight the consistency between the rock properties and the predictions of the numerical model. This suggests that the flat-joint model is well-suited for investigating uniaxial compressive strength (UCS) and tensile strength using numerical simulations.

3.2 PFC Model development

In this research, meticulous preparation was undertaken to create six layered models, each measuring 200 mm × 240 mm. These models were structured as follows: a single soft layer, single hard layer, two-layered models featuring both

Table 3 Micro parameters obtained by try and error for calibration of hard rock and soft rack

	Description	Hard rock	Soft rock
Flat jointed parameters	Young modulus (GPa)	8	5
	Friction (°)	39	32
	FJ bond tensile strength (MPa)	1.4	0.5
	Standard deviation of tensile strength (MPa)	0.14	0.05
	FJ bond cohesion (MPa)	10	5
	Cohesion standard deviation (MPa)	1	0.5
	Normal stiffness to shear stiffness ration	1.5	1.3
Particle-based parameters	Minimum particle radius (mm)	0.13	0.15
	Particle radius ratio	1.5	1.6
	Normal stiffness to shear stiffness ration	1.5	1.3
	Density (kg/m3)	2600	2400
	Young modulus (GPa)	8	5

Table 4 Mechanical properties of soft and hard material

Type	σ_c (MPa)	E (GPa)	σ_t (MPa)	σ_c/σ_t
Soft material	7.9	3.95	0.7	11.3
Hard material	12.35	8.2	1.61	7.7

(a)　　　　　(b)　　　　　(c)
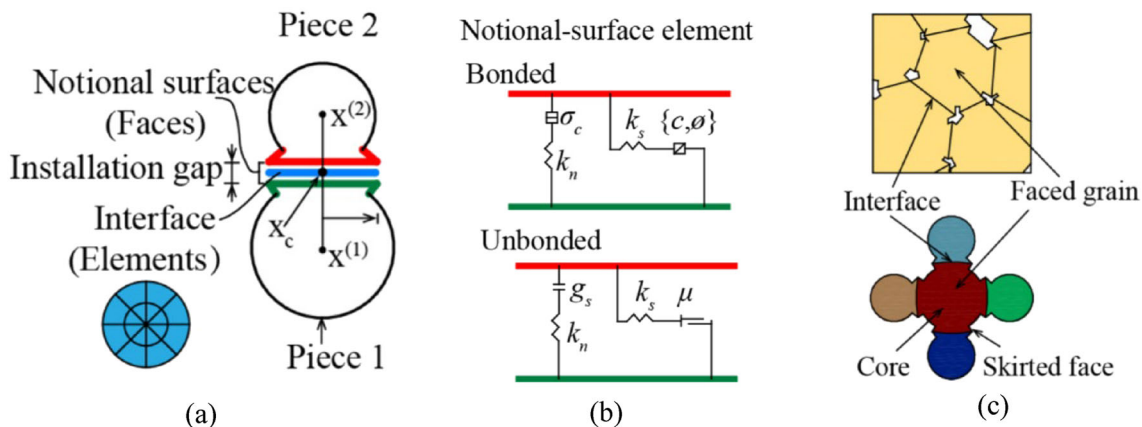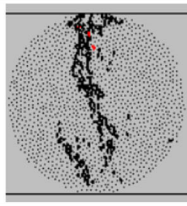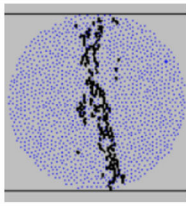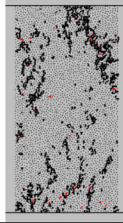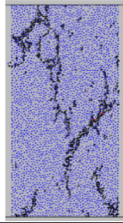
Fig. 6 Illustrates various aspects related to the research, namely: a) the contact between flat joints, **b** the rheological components involved, and **c** the material with flat joints (Potyondy 2017)
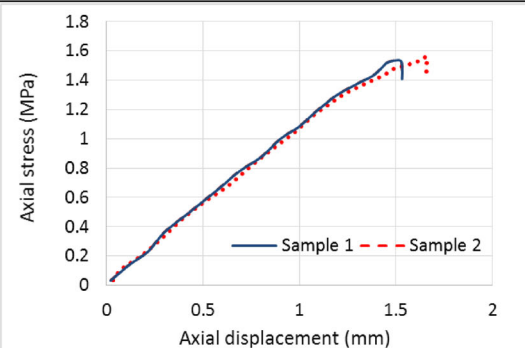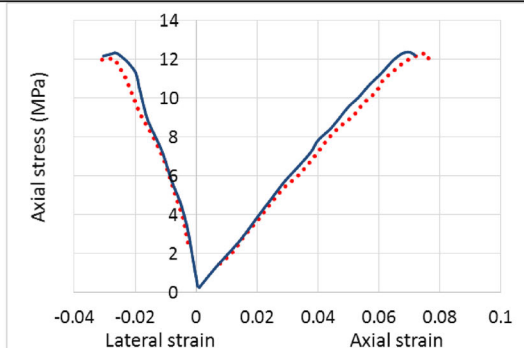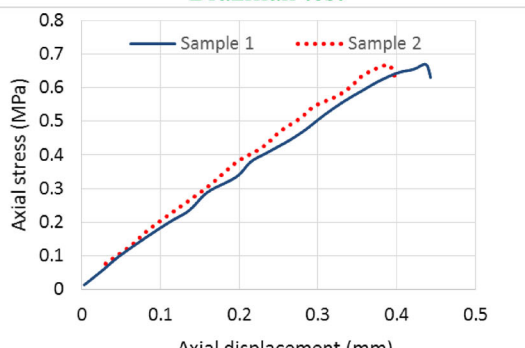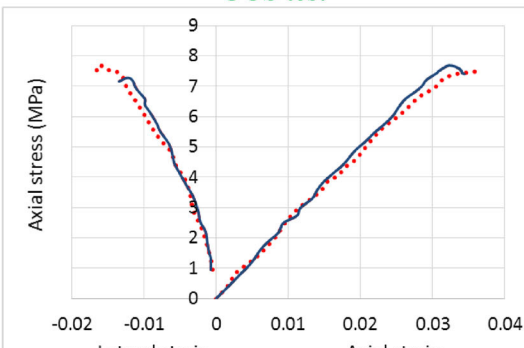
Table 5 Failure pattern of soft and hard material in experimental and numerical investigations
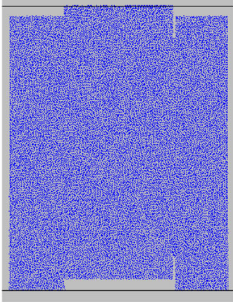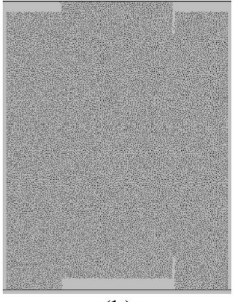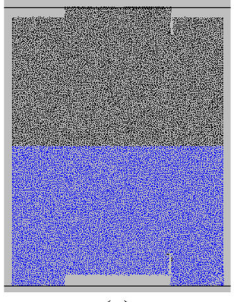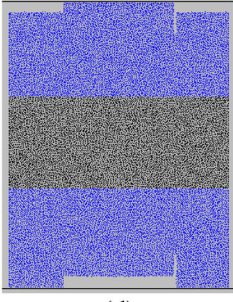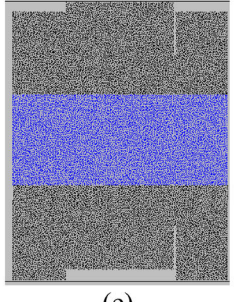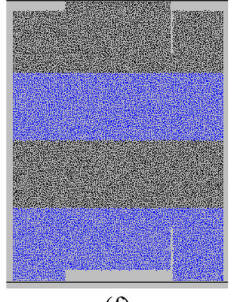
soft and hard material layers, a three-layered model with a hard interlayer, a three-layered model with a soft interlayer, and a four-layered model comprising two layers of soft and hard material. The inclination angle of the bedding layer was consistently set at 90°, as specified in Tables 6 and 7. Table 2 outlined the thickness values of the soft material for various model types. All models were furnished with

two parallel vertical edge notches, each with a width of 1 mm and a length of 20 mm, mirroring their physical counterparts. Shear test configuration was simulated as described in Table 6. The dimensions of the removal rectangles were standardized, with a width of 10 mm. The lengths of the two upper rectangles were set at 50 mm, while the middle rectangle had a length of 100 mm. For the shear test configuration

Table 6 Numerical models in absence of normal stress

One soft layer	One hard layer	Two layered model
(a)	(b)	(c)
Three layered model with hard interlayer	Three layered model with soft interlayer	Four layered model
(d)	(e)	(f)

with a normal load, two narrow horizontal bands of particles were removed from the left and right corners of the model, as detailed in Table 7. The lengths of these removal rectangles were 100 mm, and their width was 10 mm. To simulate a normal stress of 2 MPa on the models, the left and right walls were brought close to each other. This normal stress remained constant during the shear test, regulated by a servo control application code. The shear displacement was determined by monitoring the displacements of the upper wall, while the applied shear force was estimated by recording the reaction forces on the upper wall. In the punch test without a normal stress, 50% of the applied force was distributed across one shear surface, equivalent to 220 mm, due to the double shear test condition, as described in Table 6. In the shear test with a normal stress, the entire applied force was distributed across a shear surface equal to 220 mm, following the single shear test condition, as specified in Table 7. A comprehensive set of 12 models underwent shear testing, encompassing scenarios with zero normal stress and 2 MPa normal stress, with the objective of investigating acoustic emission phenomena throughout the shear displacement.

4 Numerical findings
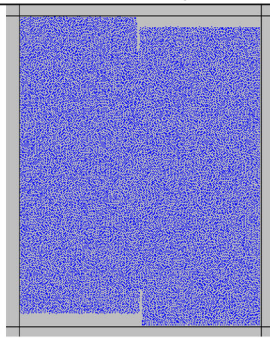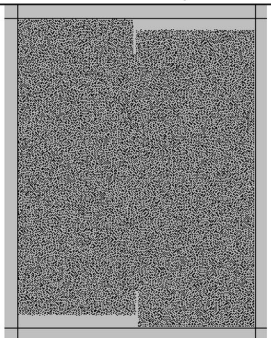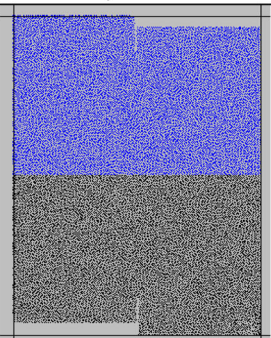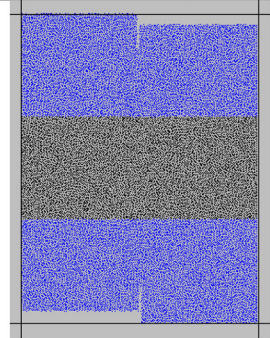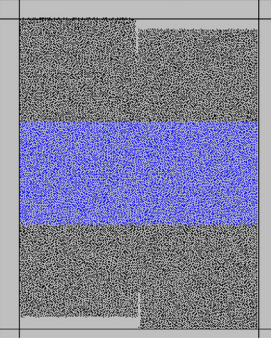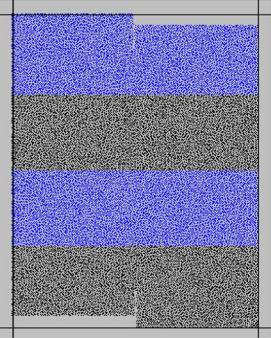
4.1 PFC validation

4.1.1 Crack growth in layered models and physical samples in absence of normal stress

Figures 7 and 8 depict the failure patterns observed in physical samples and numerical models, respectively, showcasing various numbers of horizontal bedding layers in the absence of normal stress. The hard material and soft material are denoted by gray and blue colors, respectively, while the tensile and shear cracks are represented by black and red lines, respectively. In the single-layer soft material models (Figs. 7a and 8a), as well as in the single-layer hard material models (Figs. 7b and 8b), a single tensile crack emerged from the lower fissure tip and veered left for a short distance.

In the two-layer models, a single tensile crack initiates at the lower fissure tip within the soft material layer, initially propagating leftward before transitioning parallel to the shear loading axis until reaching the interface with the hard material layer. Subsequently, it extends through the hard material layer towards its upper boundary. In the three-layer models featuring either a hard material or soft material interlayer, the crack originates from the lower fissure tip in the respective layer, briefly deviating in direction before progressing

Table 7 Numerical models under normal stress of 2 MPa

One soft layer	One hard layer	Two layered model
(a)	(b)	(c)
Three layered model with hard interlayer	Three layered model with soft interlayer	Four layered model
(d)	(e)	(f)

vertically through the layer interfaces to reach the upper fissure tip. In the four-layer model, the crack commences at the lower fissure tip within the soft material, briefly diverting leftward before propagating parallel to the shear loading direction through the layer interfaces until reaching the upper fissure tip. A comparison between Figs. 7 and 8 underscores the consistent occurrence of these failure patterns across both experimental and numerical studies.

4.1.2 Effect of horizontal layer number on the numerical and experimental shear strength

Figure 9 illustrates the shear strength variation across different layer configurations, comparing results from numerical simulations and experimental tests. The model with a single hard layer exhibited the highest shear strength, while the model with a single soft layer showed the lowest. Notably, the three-layered model with a soft interlayer displayed higher shear strength compared to the two-layered and four-layered models, as well as the three-layered model with a hard interlayer, but it remained lower than the single ductile material model.

The interaction between ductile material and brittle material on the shear surface significantly influenced shear strength variation. In the single hard model, the shear surface was entirely composed of ductile material, resulting in maximum shear strength. Conversely, the absence of hard material in the shear surface of the single soft model led to minimum shear strength. In the three-layered model with a soft interlayer, the larger coverage of hard material on the shear surface contributed to higher shear strength compared to other configurations. Similarly, the similar volume of ductile material in the shear surface of the two-layered and four-layered models resulted in comparable and higher shear strength values compared to the three-layered model with a hard interlayer.

Importantly, the shear strength values obtained from both numerical simulations and experimental testing were consistent, confirming the accuracy of the PFC software in simulating layered model failure mechanisms.

4.2 Comprehensive results obtained by PFC simulation

4.2.1 Failure patterns of numerical models under normal stress of 2 MPa

Figure 10 present the failure patterns of numerical models with different numbers of horizontal bedding layers under
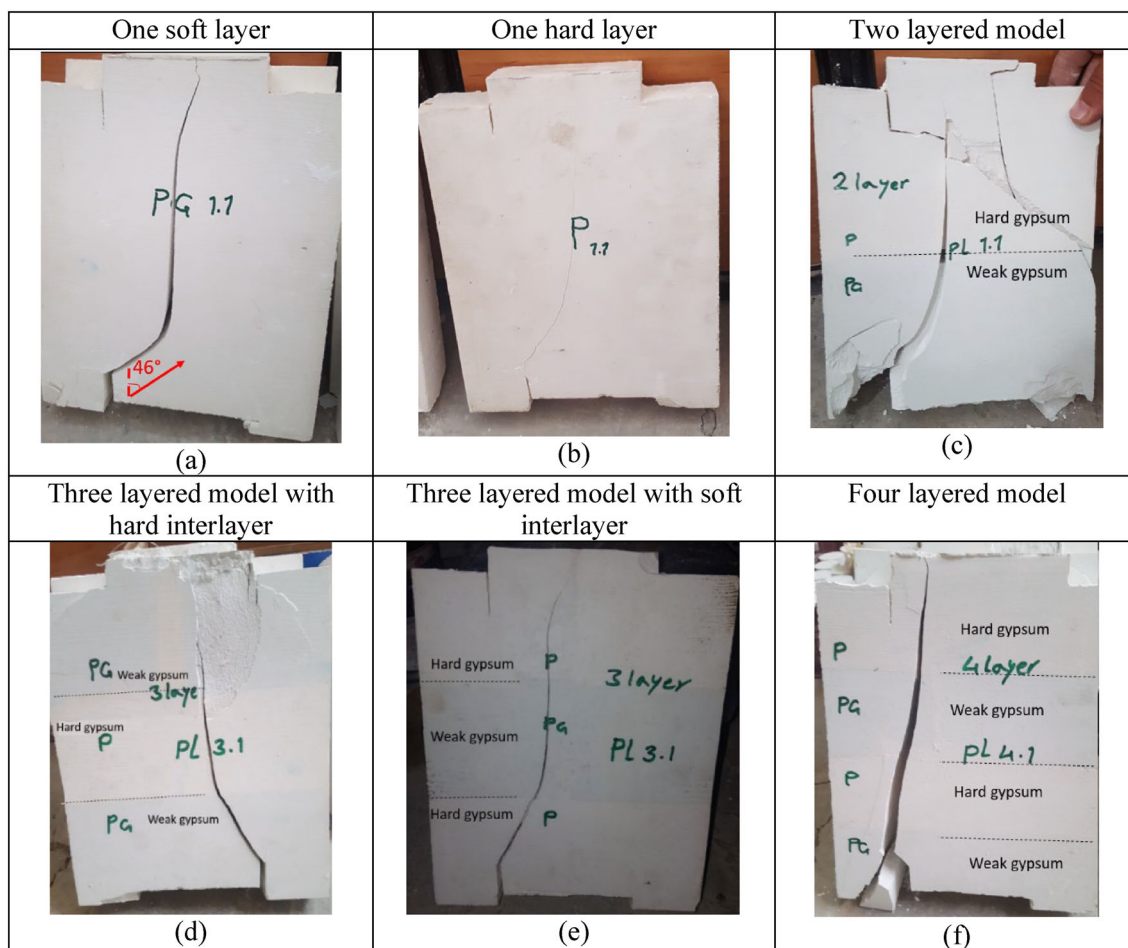
Fig. 7 The failure patterns of physical samples are depicted under various conditions: **a** comprising a single soft layer, **b** featuring a solitary hard layer, **c** representing a two-layered model, **d** showcasing a three-layered model with a hard interlayer, **e** illustrating a three-layered model with a soft interlayer, and **f** displaying a four-layered model. These patterns are observed in the absence of normal stress

normal stress of 2 MPa, the hard material and soft material are represented by the gray and blue colors respectively, while the black and red lines show the tensile and shear cracks, respectively.

In single soft layered model (Fig. 10a), two different types of fractures were observed within the model. In the first type of fracture, tensile fractures were initiated from the tips of the notches and grow parallel to the shear loading direction until reach to the center of the model. In the second type of fracture, several parallel mixed-mode (shear-tensile) fractures developed diagonally (45°) in the soft material. Tensile cracks are dominant mode of failure that occurs in the model. In single hard layered model (Fig. 10b), three two types of fractures were observed within the model. In the first type of fracture, tensile fractures were initiated from the tips of the notches and grow parallel to the shear loading direction until reach to the center of the model. In the second type of fracture, several parallel mixed-mode (shear-tensile) fractures developed diagonally (45°) in the hard material. Tensile

cracks are dominant mode of failure that occurs in the model. By comparison between Fig. 10a and b, it's clear that the length of diagonal fractures were increased by increasing the brittleness of model in soft material.

In two layered model (Fig. 10c), four different types of fractures were observed within the model. The first type of fracture involved vertical tensile fractures that were initiated from the tip of the upper fissure in the soft material and grow parallel to the shear loading direction downward until coalescence with the horizontal interface. The second type of fracture involved several parallel mixed-mode fractures that developed diagonally (45°) in the soft material. In the third type of fracture, tensile fractures were initiated from the tip of the lower fissure in the hard material and grow parallel to the shear loading direction upward until coalescence with the horizontal interface. In the fourth type of fracture, several parallel mixed-mode fractures were developed diagonally (45°) in the hard material.

Fig. 8 Failure pattern of models containing single soft layer, single hard layer, two layered model, model with hard interlayer, model with soft interlayer and four layer; in absence of normal stress
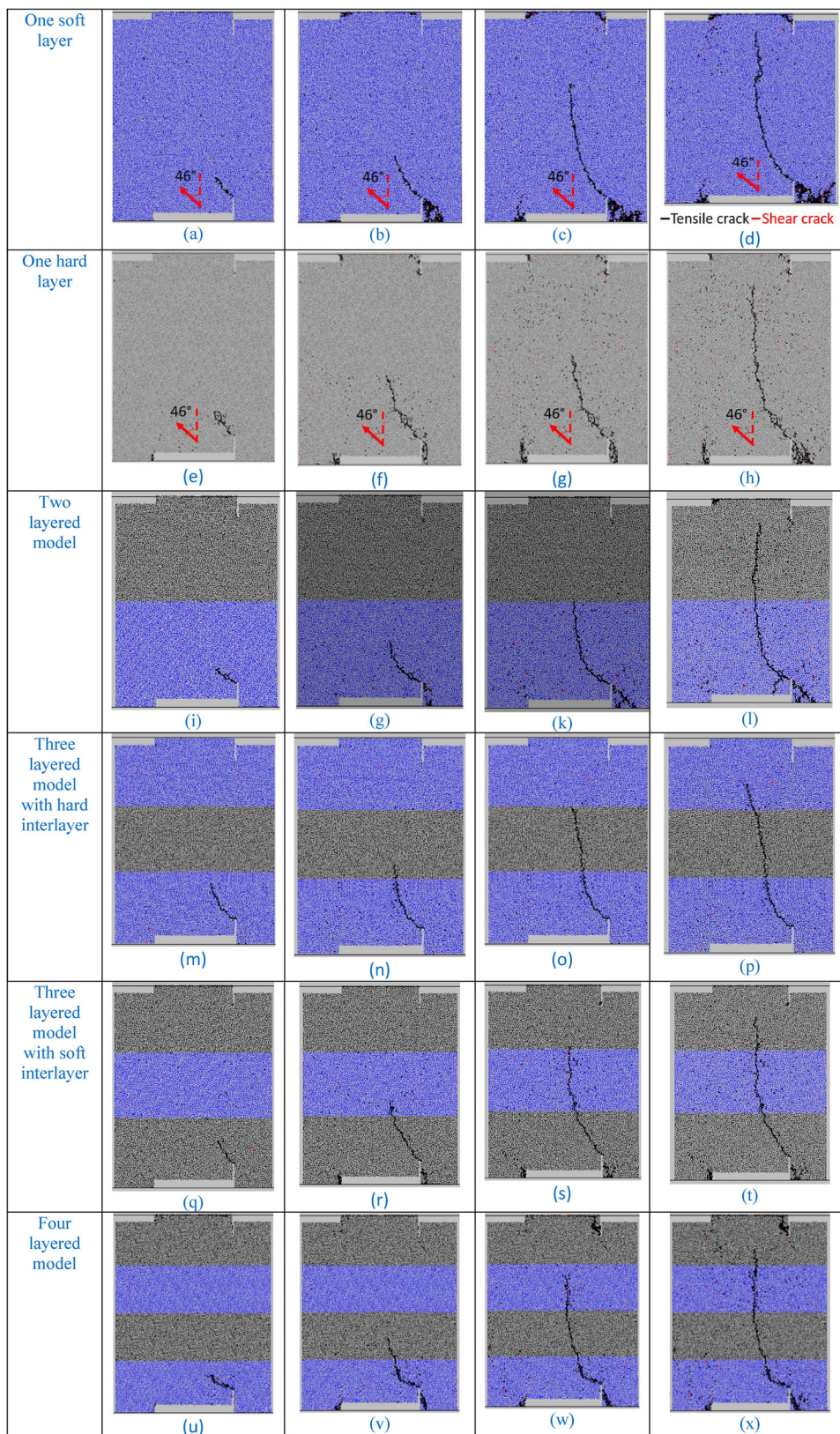
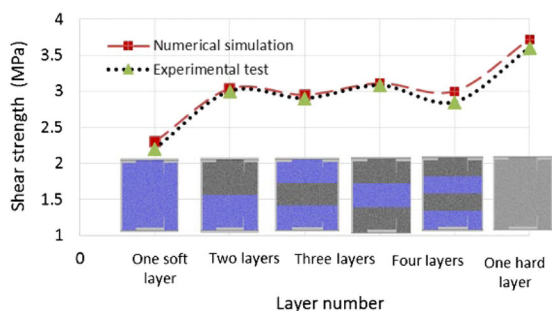**Fig. 9** Variation of shear strength based on layer number; experimental results and numerical outputs

In model with hard interlayer (Fig. 10d), three different types of fractures were observed within the model. In the first type of fracture, tensile fractures were initiated from the tips of the notches in soft material and grow almost parallel to the shear loading direction until coalescence with the layer interfaces. In the second type of fracture, tensile fractures were initiated from both interfaces and grow diagonally in the middle hard layer. In the third type of fracture, several parallel mixed-mode fractures developed diagonally (45°) in the both of the soft and hard layers.

In model with soft interlayer (Fig. 10e), three different types of fractures were observed within the model. In the first type of fracture, tensile fractures were initiated from the tips of the notches in hard material and grow almost parallel to the shear loading direction until coalescence with the layer interfaces. In the second type of fracture, tensile fractures were initiated from both interfaces and grow diagonally in the soft layer. In the third type of fracture, several parallel mixed-mode fractures developed diagonally (45°) in the both of the soft and hard layers.

In four layer (Fig. 10f), three different types of fractures were identified within the model. In the first type of fracture, two tensile fractures were initiated from the upper and lower boundaries of the soft and hard layers, respectively. These fractures grow almost parallel to the shear loading direction until coalescence with the layer interfaces. In the second type of fracture, several small parallel shear bands developed diagonally (45°) in both the upper soft interlayer and lower hard interlayer. In the third type of fracture, several small parallel shear bands developed diagonally (45°) in both the hard interlayer and soft interlayer.

By comparison between Fig. 10a–f, it is clear that the length of diagonal fractures in brittle layer was more than that in hard material layer due to brittleness effect of soft material.

4.2.2 Effect of normal stress and model brittleness on the acoustic emission phenomena

As stated by Shi et al. (2022), the phenomenon of acoustic emission takes place when a material undergoes stress concentration, leading to the rapid release of energy and the generation of transient elastic waves. In this research, the meaning of major AE hits is associated to large crack number initiated in the model. In other word, cracks were initiated in rock bridge during shear loading. When differences between numbers of cracks in two neighboring steps increased remarkably, one major AE hits will be occurred. Unit of AE is number. In fact the acoustic emission hits were registered during the test.

In this particular section, the authors investigate the relationship between the quantity of acoustic hits and the number of horizontal bedding layers from the initiation of shear stress on the bedding layer to the ultimate failure of the rock bridge, considering two distinct normal stress levels.

(a) Acoustic emission phenomena without present of normal stress

This study examines the relationship between acoustic emission events and the number of horizontal bedding layers during the entire process, from the application of shear stress on the bedding layer to the ultimate failure of the rock bridge, without considering the presence of normal stress.

(a.1) Acoustic emission single soft layer

Figure 11a illustrates the acoustic emission patterns in a soft material layer, showing three stages: relative calm (stage I), crack initiation and growth (stage II), and final failure (stage III). In stage I, few Acoustic hits with high continuity indicate minimal microcrack initiation. Stage II sees more Acoustic hits, suggesting crack propagation. Stage III shows fewer, shorter Acoustic hits, indicating greater energy release. Major Acoustic hits increase with shear displacement, implying higher energy release during final failure than crack initiation. The number of events associated with shear movements of 0.4 mm, and 0.7 mm were 9 and 11, respectively, indicating higher energy release in the final failure stage. The initiation of a new crack in the ductile layer required more energy, resulting in a higher release during the first major event. Subsequent events showed variations in energy release depending on crack propagation conditions.

(a.2) Acoustic emission in single hard layer

Figure 11b displays acoustic emission properties of a hard layer with various fissure lengths, following a similar pattern observed in a single soft layer. Divided into three stages (quietness, crack initiation and growth, final failure), two significant acoustic event peaks mark crack initiation and unstable propagation. Compared to the soft layer (Fig. 11a), the firm layer (Fig. 11b) shows higher shear displacement for
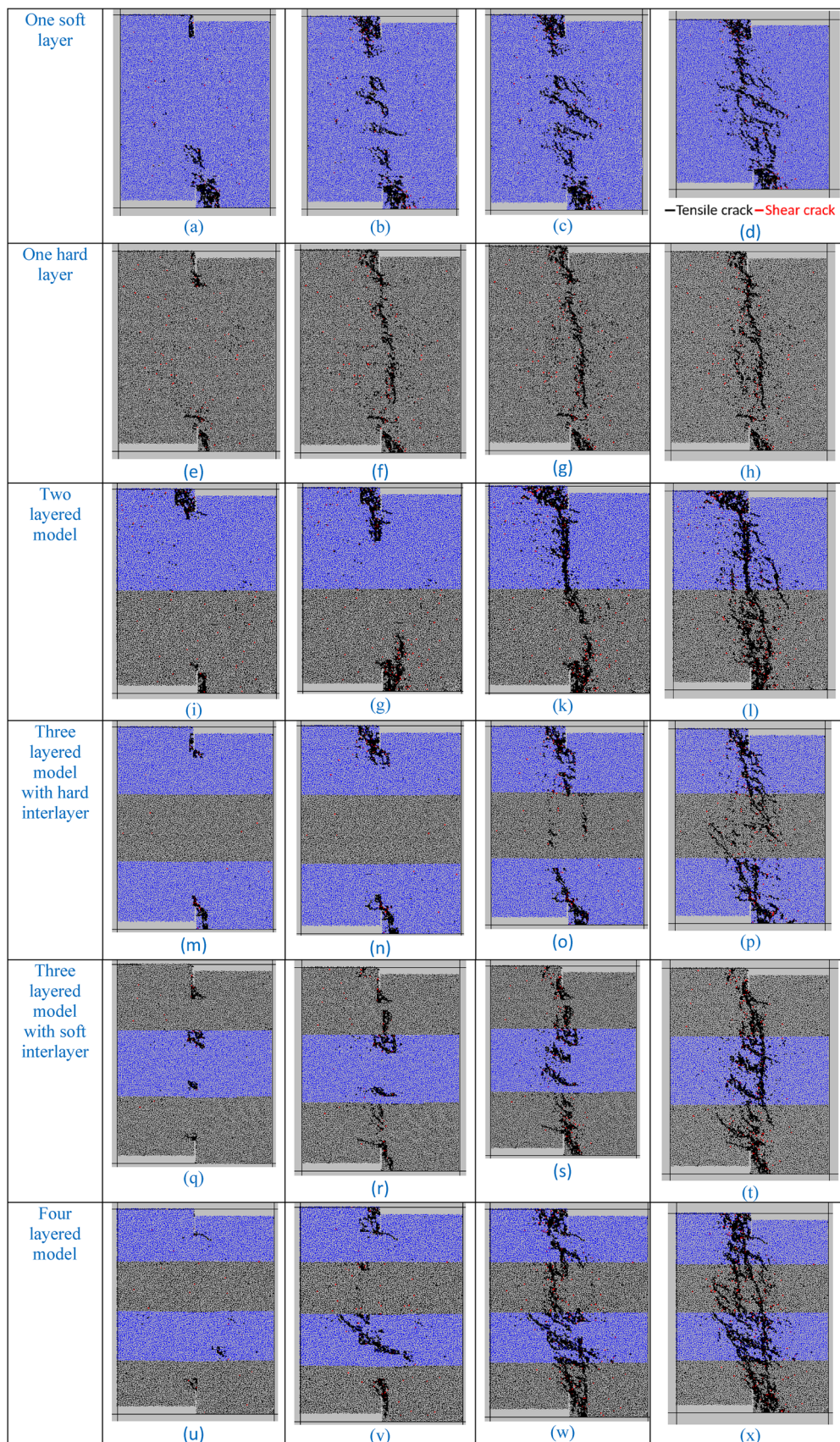
Fig. 10 Failure pattern of models containing single soft layer, single hard layer, two layered model, model with hard interlayer, model with soft interlayer and four layer; under normal stress of 2 MPa

stage II initiation and stage III onset. This reflects the firm layer's ductile nature, with a lower compression-to-tensile strength ratio. Despite its deformability, the firm layer experiences brittle failure, releasing more energy during final failure. Major Acoustic hits increase with shear displacement, indicating higher energy release during final failure than crack initiation. The firm layer exhibits more Acoustic hits during rock bridge failure due to stronger particle cementation, requiring more energy for crack propagation. Increasing fissure length reduces acoustic event hits, minimizing discrepancies in major acoustic event numbers with constant mechanical properties. The number of events associated with shear movements of 0.42 mm, and 0.95 mm were 15 and 19, respectively, indicating higher energy release in the final failure stage.

(a.3) Acoustic emission in two layered model

Figure 11c shows AE behavior in a two-layered model with horizontal bedding, dividing the process into four stages: silence (stage I), crack initiation and growth (stage II), initial interface breakage (stage III), and ultimate failure (stage IV). These stages saw three significant Acoustic hits. In stage II, a notable peak occurred early at 0.35 mm shear movement, originating from the lower fissure tip in the brittle material layer. Stage III showed greater continuity due to the tensile crack propagating through the hard, ductile material and the brittle interlayer material. The third major acoustic event, at 0.73 mm shear displacement in stage IV, signaled a higher energy release, indicating the initiation of a new crack in the brittle layer. The second significant acoustic event surpassed the first in energy, and the third exceeded both, reflecting the substantial energy required for complete penetration of the hard, ductile layer by the tensile crack.

(a.4) Acoustic emission in model with hard inter layer

In Fig. 11d, acoustic event properties of models with a hard interlayer are depicted, dividing the process into five stages: initial quietness, crack initiation and growth, first and second interface breakage, and final failure (I, II, III, IV, V). Four distinct Acoustic hits were observed across these stages. In stage I, a significant acoustic event peak occurred at the start of stage II, originating from a tensile crack initiation in the brittle material layer. Subsequently, a second notable acoustic event peak emerged in stage III, indicating uniform microcrack generation. Stage III showed higher continuity than stage II due to tensile crack propagation through the hard, ductile material. The third major acoustic event occurred in stage IV, with greater released energy during final failure compared to other stages. Initiation of a new crack in the hard, ductile layer required more energy for the second major acoustic event, resulting in higher released energy. The fourth major acoustic event, associated with final failure, exhibited lower energy as less energy was needed for crack propagation in brittle material.

(a.5) Acoustic emission in model with soft interlayer

In Fig. 11e, acoustic emission properties of three horizontally layered models with a flexible interlayer are shown, divided into five stages: silence (I), crack initiation and growth (II), first interface breakage (III), second interface breakage (IV), and ultimate failure (V). Four distinct acoustic emission events were observed. In stage I, minimal activity with consistent continuity was noted. At the start of stage II, a significant peak was observed at a shear movement of 0.46 mm, indicating tensile crack initiation from the lower fissure tip in the ductile material layer. Subsequently, signals increased uniformly, indicating microcrack generation. In stage III, the second major peak occurred at a shear movement of 0.68 mm, with lower continuity compared to stage II due to crack propagation through the soft, brittle interlayer material. Stage IV exhibited the third major activity at 0.75 mm shear movement, with higher continuity than stage III as the crack extended through the ductile material. The fourth major event, marking final failure, occurred at the start of stage V with a shear movement of 0.86 mm, exhibiting weaker continuity. The number of events associated with shear movements of 0.46 mm, 0.68 mm, 0.75 mm, and 0.86 mm were 12, 9, 14, and 17 respectively, indicating higher energy release in the final failure stage. The initiation of a new crack in the ductile layer required more energy, resulting in a higher release during the first major event. Subsequent events showed variations in energy release depending on crack propagation conditions.

(a.6) Acoustic emission in four layer

In Fig. 11f, acoustic emission patterns of a four-layered horizontally arranged model are shown, covering six stages: silence (I), crack onset and growth (II), initial, second, and third interface breakage (III, IV, V), and final failure (VI). Across these phases, four notable acoustic emission occurrences were observed. Phase I showed minimal yet continuous acoustic emission. The first significant peak appeared at the beginning of Phase II, indicating crack initiation in the soft, brittle layer's lower fissure tip. Phase III displayed increased activity, with crack propagation mainly through the firm, ductile interlayer material. Another notable event occurred at the start of Phase IV, with continuity exceeding that of Phase III as the crack go through the soft, brittle layer. The fourth significant event occurred at the beginning of Phase IV, with higher continuity due to crack propagation through the firm, ductile material layer. The number of events associated with shear movements of 0.38 mm, 0.42 mm, 0.62 mm, and 0.7 mm were 10, 12, 15, and 18, respectively, indicating escalating energy release during final failure. These acoustic emission features offer insights into
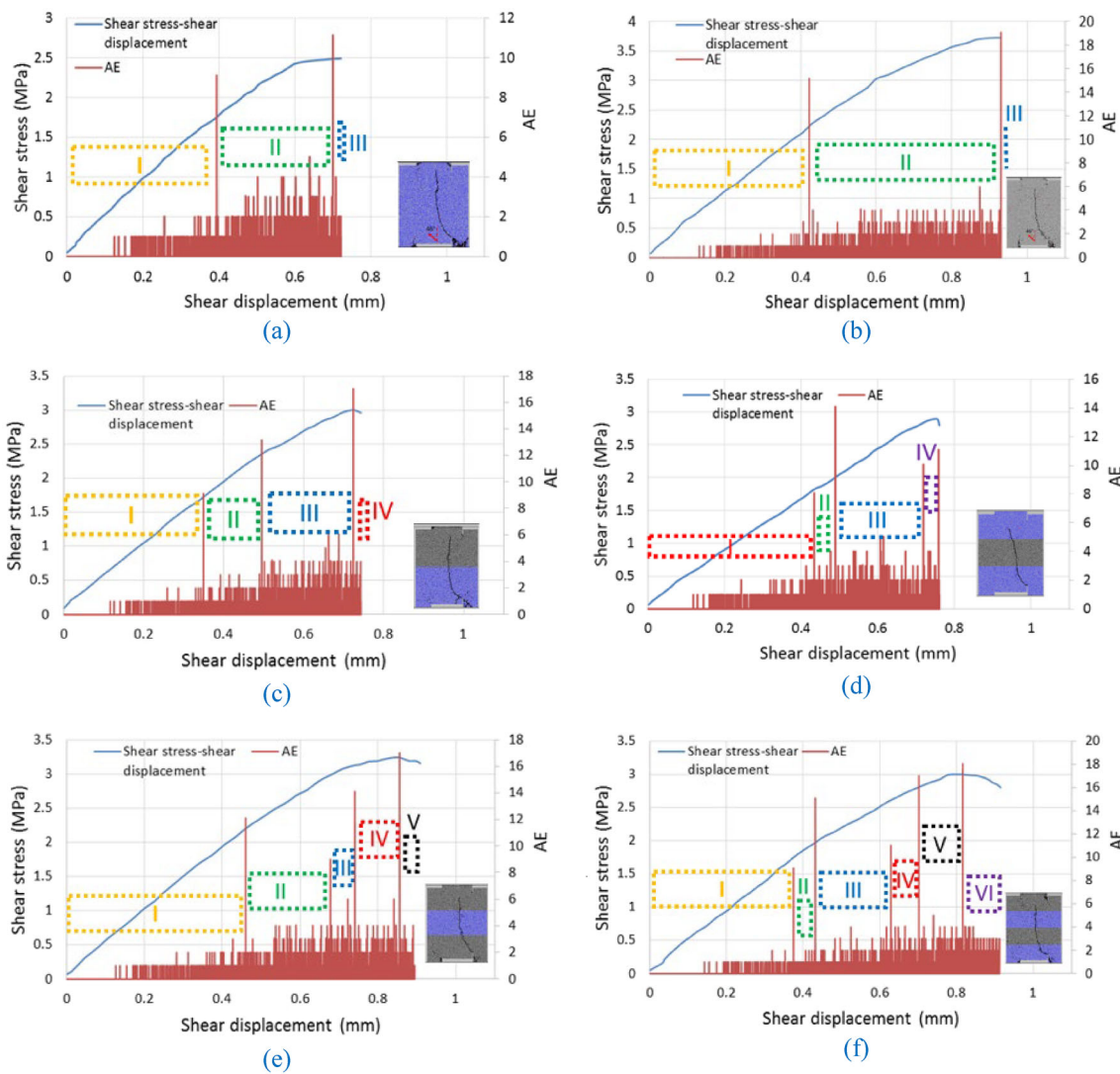
Fig. 11 Acoustic emission hits in models containing, **a** single soft layer, **b** single hard layer, **c** two layered model, **d** model with soft interlayer and **e** four layer

failure and deformation behaviors of layered models, aiding in assessing their mechanical response and stability.

(b) Acoustic emission phenomena with present of normal stress of 2 MPa

This segment explores the connection between acoustic emission occurrences and the number of horizontal bedding strata throughout the entire sequence. The procedure begins with the imposition of shear strain on the bedding stratum and ends with the collapse of the rock span under a perpendicular stress of 2 MPa.

(b.1) Acoustic emission in single soft layer

As shown in Fig. 12a, the Acoustic Emission process in a soft, brittle layer follows three stages: initial silence (stage I), crack initiation and growth (stage II), and final failure (stage III). This acoustic event behavior mirrors that of a single

soft, brittle layer without a normal load (Fig. 12a). Comparing Figs. 11a and 12a reveals an increase in shear movement associated with Acoustic hits as normal stress rises. Additionally, higher normal stress correlates with more Acoustic hits, indicating greater released energy.

(b.2) Acoustic emission in single hard layer

Figure 12b depicts the acoustic emission process in a firm layer. Like the acoustic event behavior observed without a vertical load (Fig. 11b), this process unfolds in three stages: initial silence (stage I), crack initiation and steady growth (stage II), and eventual failure (stage III). Comparing Figs. 11b and 12b suggests that as the vertical stress increases, the shear movement associated with Acoustic hits also rises. Moreover, higher vertical stress corresponds to more Acoustic hits, indicating greater energy release. Comparing Fig. 12a and b, acoustic event intensity in the pliable
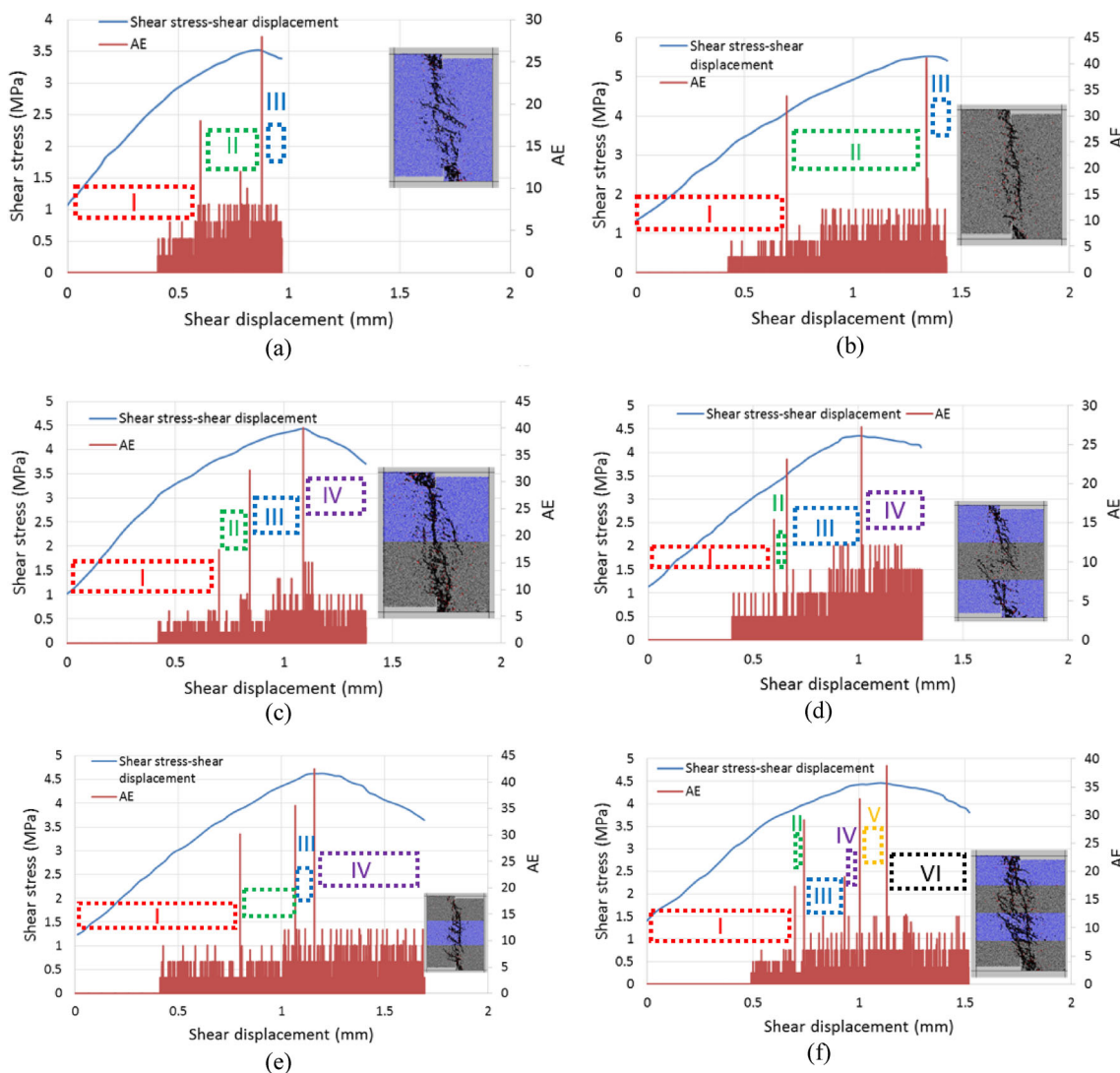
Fig. 12 Depicts acoustic emission hits in models with various configurations, **a** single soft layer, **b** single hard layer, **c** two layered model, **d** model with soft interlayer and **e** four layer; under normal stress of 2 MPa

model is lower than in the firm model. For instance, the number of events related to the first major acoustic event is 18 in the pliable model (at a shear movement of 0.618 mm in Fig. 12a) and 34 in the firm model (at a shear movement of 0.7 mm in Fig. 12b). Similarly, for the second major acoustic event, there are 27 events in the pliable model (at a shear movement of 0.88 mm in Fig. 12a) and 40 events in the firm model (at a shear movement of 1.35 mm in Fig. 12b). This indicates that acoustic event during significant crack propagation is lower in the pliable layer due to its increased flexibility. Additionally, the difference in shear movements associated with the two major acoustic event peaks is smaller in the pliable model (0.262 mm in Fig. 12a) than in the firm model (0.65 mm in Fig. 12b), suggesting rapid failure after crack initiation in the pliable model compared to delayed failure in the firm model. Comparing Figs. 11b and 12b also

reveals that as the vertical stress increases, the magnitude of shear movement linked to Acoustic hits rises, along with an increase in the number of Acoustic hits, indicating higher energy release.

(b.3) Acoustic emission in two layered model

Figure 12c shows the acoustic event process in a two-layered model, split into four stages: initial quiet (I), crack initiation (II), interface rupture (III), and final failure (IV). Three notable Acoustic hits occurred. Stage I had few Acoustic hits but high continuity. The first major acoustic event peak appeared in stage II at 0.7 mm shear movement, with uniform signals. The second peak was in early stage III at 0.84 mm, and the third in early stage IV at 1.1 mm. Stage III showed higher continuity than II. Failure started with vertical tensile fractures from the upper soft layer fissure, propagating

to the interface at 0.14 mm. Then, a crack from the interface extended parallel to the shear direction until the model's lower edge, and mixed-mode fractures developed in the hard layer at 0.26 mm. Due to the soft layer's lower deformability, stage III had higher continuity than stage II. The number of Acoustic hits for shear movements of 0.7 mm, 0.84 mm, and 1.1 mm were 17, 32, and 40, respectively, indicating higher energy release at final failure. Comparing Figs. 11c and 12c, higher normal stress led to increased acoustic event occurrences, suggesting greater energy release.

(b.4) Acoustic emission in model with hard interlayer

Figure 12d shows the acoustic event process in a three-layered horizontal model, divided into four stages: initial silence (stage I), crack initiation and growth (stage II), first interface rupture (stage III), and final failure (stage IV). Three significant Acoustic hits occurred. In stage I, Acoustic hits were sparse yet continuous. The first major acoustic event peak occurred at the start of stage II (shear movement: 0.54 mm), showing consistent growth with strong continuity. The second major acoustic event peak occurred early in stage III (shear movement: 0.59 mm), followed by the third at the onset of stage IV (shear movement: 1 mm). Stage III exhibited higher continuity than stage II. Failure initiated with vertical tensile fractures from notches in the soft material layer (shear movement: 0.05 mm). In the subsequent fracturing stage, a tensile crack originated from layer interfaces and propagated vertically within the middle hard layer, merging with other fractures. Mixed-mode fractures developed diagonally within the layers (shear movement: 0.41 mm). Stage II displayed lower continuity than stage III due to the brittle material layer's lower deformability compared to the ductile material layer. The number of Acoustic hits associated with shear movements of 0.54 mm (first major acoustic event), 0.59 mm (second major acoustic event), and 1 mm (third major acoustic event) were 15, 23, and 27, respectively. This indicates higher energy release during final failure, characterized by oriented shear band propagation. The energy required for crack initiation (first major acoustic event) was relatively low, resulting in a lower energy release. The third major acoustic event during final failure exhibited a higher energy release compared to the other major Acoustic hits. Comparing Figs. 11d and 12d reveals an increase in shear movement associated with acoustic event occurrences with higher normal stress. Additionally, Acoustic hits increased with elevated normal stress, indicating a larger energy release.

(b.5) Acoustic emission in model with soft interlayer

Figure 12e displays the acoustic emission process in a three-layered horizontal model, divided into five stages: initial quiet phase (stage I), crack initiation (stage II), first interface breakage (stage III), second interface breakage (stage IV), and final failure (stage V). Three significant Acoustic hits occurred during these stages. In stage I, Acoustic hits were sparse but continuous. The first major acoustic event peak appeared early in stage II, correlating with a shear movement of 0.8 mm, displaying uniform intensity. The second major acoustic event peak occurred at the onset of stage III (shear movement: 1.06 mm), followed by the third major acoustic event at the beginning of stage IV (shear movement: 1.16 mm). The failure mechanism involved vertical tensile fractures originating from notches in the hard material layer, merging with layer interfaces, and subsequent propagation. This was followed by fractures originating from layer interfaces, propagating vertically within the middle soft layer until merging with other fractures, along with diagonal fractures within layers. Stage III exhibited lower continuity than stage II due to the brittle material layer's lower deformability compared to the ductile material layer. The number of Acoustic hits associated with shear movements of 0.8 mm, 1.06 mm, and 1.16 mm were 30, 35, and 42, respectively, indicating higher energy release during final breakage. Comparing Figs. 11e and 12e, it's evident that acoustic event occurrences increase with normal stress, indicating a larger released energy under elevated normal stress conditions.

(b.6) Acoustic emission in four layer

Figure 12f displays the acoustic event process within a four-layered horizontal model, divided into six stages. Minimal Acoustic hits but continuous activity characterized stage I, while the first major acoustic event peak emerged early in stage II at 0.697 mm shear movement. Stage III saw the second major acoustic event peak at 0.74 mm shear movement, surpassing stage II's continuity due to differences in layer deformability. The third major acoustic event occurred at the start of stage IV, at 0.93 mm shear movement. Stage III's continuity exceeded that of stage IV. The fourth major acoustic event emerged at the beginning of stage IV, with a shear movement of 1 mm. Stage IV saw tensile fractures originating from the first lower interface and propagating diagonally within the soft material layer, while stage III saw propagation through the ductile layer. The fifth major acoustic event occurred at the onset of stage V, linked to a shear movement of 1.13 mm. The number of Acoustic hits associated with shear movements of 0.697 mm, 0.74 mm, 0.93 mm, 1 mm, and 1.13 mm were 17, 29, 19, 32, and 38, respectively. The thicker ductile layer in the three-layered model led to more Acoustic hits due to higher energy requirements for crack growth. Comparing Figs. 11f and 12f, acoustic event occurrences increased with higher normal stress, indicating a larger energy release.
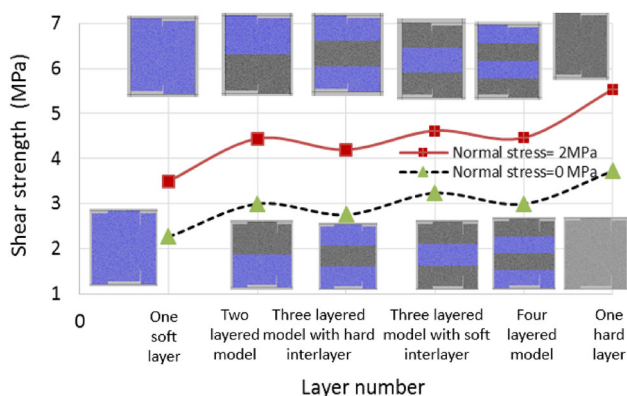
Fig. 13 Effect of layer number and normal stress on the shear strength of model

4.2.3 Effect of layer number and model brittleness on the shear strength

Figure 13 demonstrates the effect of layer count and perpendicular stress on shear strength. The highest and lowest shear strength values were observed in setups with a single rigid layer and a single pliable layer, respectively. Configurations with three layers, including a pliable interlayer, showed higher shear strength compared to those with two, four, and three layers with a rigid interlayer. However, their shear strength remained lower than that of setups with a single layer of rigid material. The presence of both rigid and pliable material significantly influenced shear strength variations on the shear surface. In setups with a single rigid layer, the entire shear surface comprised rigid material, resulting in the highest shear strength. Conversely, setups with a single pliable layer had the lowest shear strength due to the absence of rigid material on the shear surface. Remarkably, setups with a pliable interlayer had a greater proportion of rigid material on the shear surface compared to setups with a rigid interlayer. This contributed to their increased shear strength. The shear strength of setups with two and four layers was similar, as they had comparable volumes of rigid material on the shear surface, both higher than setups with a rigid interlayer. Numerical simulations and experimental tests yielded consistent results regarding shear strength values. Additionally, there was a positive relationship between shear strength and normal stress, as an increase in normal stress corresponded to an increase in shear strength.

4.3 Particle displacement trend with and without presence of normal stress

Figures 14 and 15 show particle displacement trend in 6 models with different layer configurations with and without presence of confining pressure, respectively. The displacement vectors of the particles in a given PFC assembly illustrate how the particles are moving as they are subjected to the external loading conditions. In absence of normal stress (Fig. 14), displacement vectors are perpendicular to crack grow path. This is a major evidence of tensile crack propagation in rock bridge in absence of normal stress. Because as can be seen in Fig. 16, particle displacement trend in an indirect tensile test simulation are same as displacement trends in the punch test. As shown in Fig. 14, despite the unique differences in the stress paths between the punch test and the indirect tensile test, the displacement directions show similar trends, and the failure display an opening phenomenon, characteristic of tensile fractures, i.e., the fracture mechanics terminology for failure under tensile loading.

Under high normal stress (Fig. 15), displacement vectors have two different directions i.e. perpendicular to crack grow path and parallel to crack grow direction. This is a good evidence that both of the tensile cracks and shear cracks developed through the rock bridge. In other word, shear cracks that occur due to sliding movement of suppressed particles along the shear surface have parallel displacement vector regarding to crack grow path.

5 Discussion

This research explores how normal stress affects the strength, failure patterns, and acoustic emissions of rocks with different layers during shear tests. It looks at the mechanical properties of the bedding layer, the number of layers, and the thickness ratios of hard and soft rocks. We used punch-through tests and PFC2D for this study.

The properties of the bedding layer play a big role in the movement between two consecutive acoustic events. Soft and brittle material, compared to hard and ductile material, is less deformable, leading to less consistent movement in the soft layer. These factors impact the strength of a layered model, with soft material being weaker than hard material. The highest strength is seen when hard material covers more of the shear surfaces. Under zero normal stress, models with different layers had varying numbers of acoustic events. The number of layer interfaces correlates with the number of significant acoustic events, increasing as the layers in a sample grow.

The consistency of acoustic events between two major occurrences is related to how brittle the model is. Acoustic signals are more evident in rigid and malleable material compared to pliable and fragile material, primarily because of the ratio of compressive strength to tensile strength in the rigid and malleable stratum. The stress intensity in rigid and malleable material primarily contributes to deforming the crack tip, demanding greater energy for crack extension, thus leading to more significant acoustic occurrences. Under 2 MPa normal stress, acoustic events were similar to models without
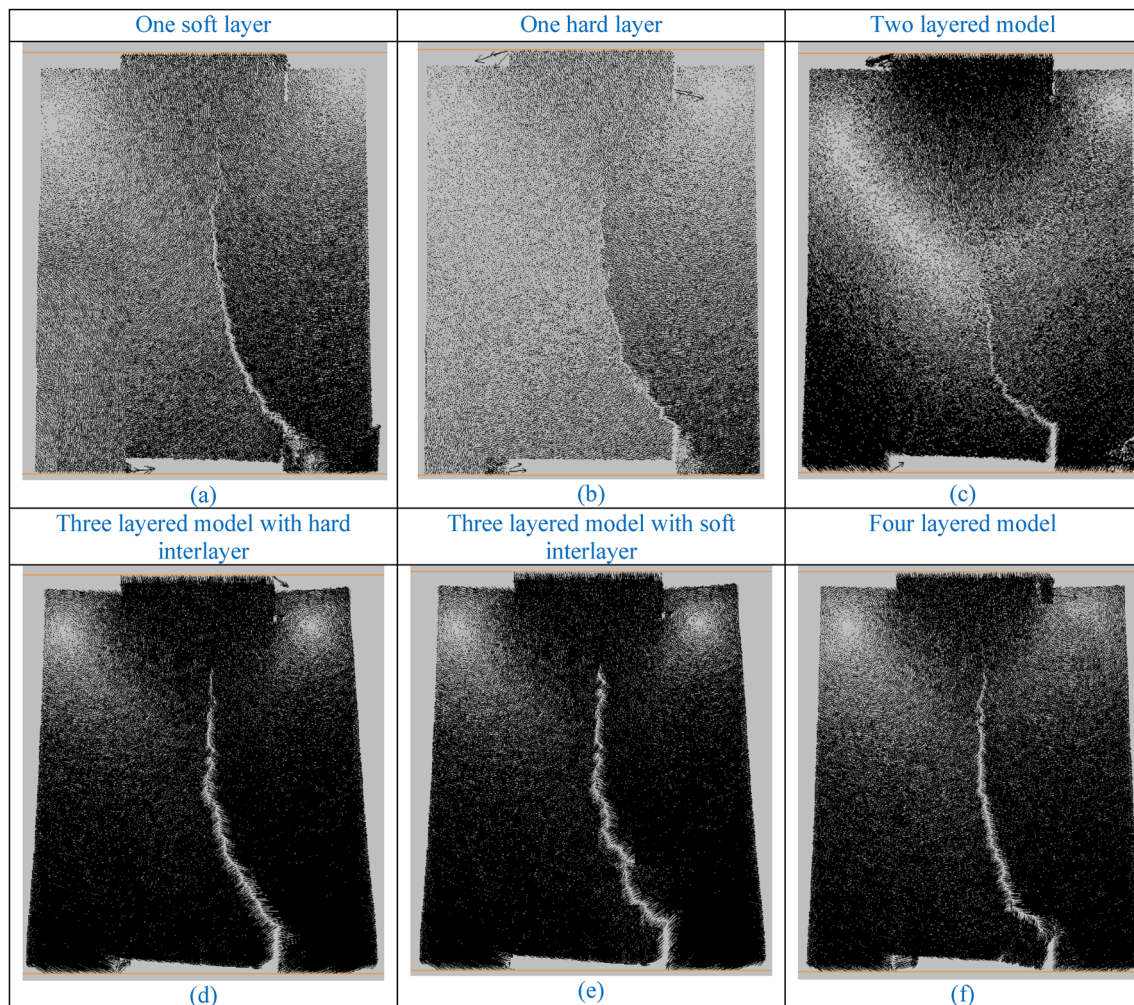
Fig. 14 Displacement vectors of numerical models are depicted under various conditions: **a** comprising a single soft layer, **b** featuring a solitary hard layer, **c** representing a two-layered model, **d** showcasing a three-layered model with a hard interlayer, **e** illustrating a three-layered model with a soft interlayer, and **f** displaying a four-layered model. These patterns are observed in the absence of normal stress

normal stress, but the number of events decreased with more stress. The intensity and consistency of events increased with normal stress due to the compaction of the rock model under 2 MPa.

This study investigates how rock brittleness affect layered rock's shear failure process. The study primarily looks at how these factors impact rock bridges that fracture quickly or those fail slowly. The findings show that presence of hard bedding layer in shear direction improves the rock bridge's shear rigidity. When the thickness of hard layer increases, the elastic stage's duration increases and the first significant acoustic emission (AE) event occurs at a larger shear displacement. Additionally, the research finds that the tensile stress at the notch tip greatly surpasses the tensile strength of the soft gypsum, resulting in the beginning of additional tensile cracks at the notch tip. This emphasizes how important

stress concentration and hard layer thickness are in determining how layered rock that is subjected to shear conditions behaves in terms of fracture and failure mechanism.

Substantial AE events are strongly associated with crucial phases, including interface breakage, final rupture, and crack initiation. Furthermore, throughout the failure process, variables including the layer thickness and material brittleness are critical in determining the frequency and intensity of AE occurrences. An increase in the total number of major AE events is seen when the number of layers in a material sample is raised, suggesting that there is a positive association between the number of layer interfaces and the incidence of large AE events. Since soft brittle gypsum and hard ductile gypsum are present on the shear surface, controlling the AE continuity change in the bedding layer, the bedding angle appears to have an impact on the continuity of AE events between two main AE events.
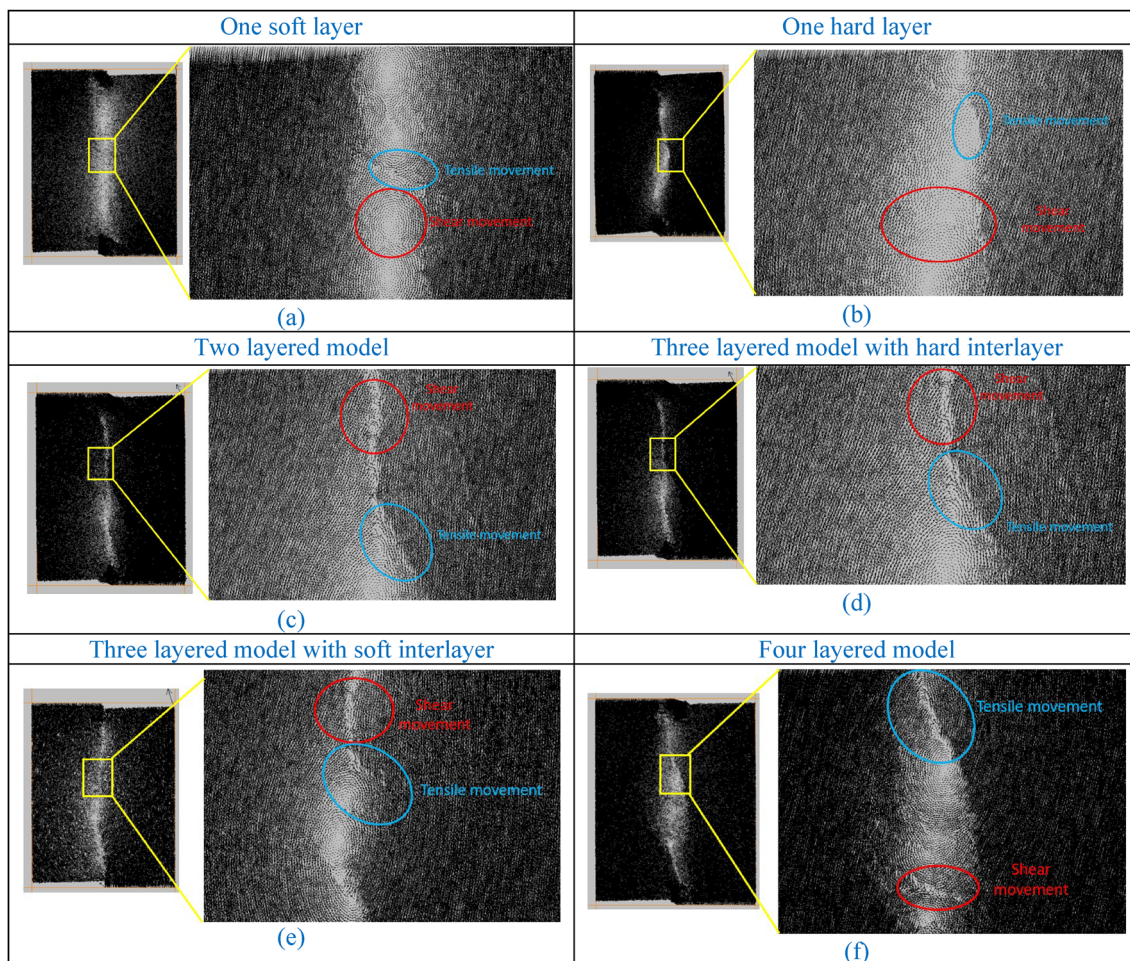
Fig. 15 Displacement vectors of numerical models are depicted under various conditions: **a** comprising a single soft layer, **b** featuring a solitary hard layer, **c** representing a two-layered model, **d** showcasing a three-layered model with a hard interlayer, **e** illustrating a three-layered model with a soft interlayer, and **f** displaying a four-layered model. These patterns are observed in presence of normal stress

Ductile layer's shear stiffness is greater than the soft brittle layer's when the hard, ductile gypsum was more prevalent on the shear surface. This lead to the shear displacement associated with the last big AE event grew. This shows that the rock bridge had delayed failure following the onset of cracks in one hard layered rock. The shear displacement associated with the last major AE event increased as the hard ductile layer's shear stiffness exceeded the soft brittle layer's. This suggests that the rock bridge had delayed collapse following the onset of cracks.

The study highlights a close association between the hard layer thickness and the continuation of acoustic emission events. An increase in the soft layer thickness decreased the rock bridge stiffness so delayed failure change to rapid fracturing. Hard ductile gypsum exhibits more acoustic emission than soft brittle gypsum. This difference is explained by the hard-ductile layer's reduced ratio of tensile strength to compression strength. In hard ductile gypsum, the main purpose

of stress intensity at the fracture tip is to deform the crack tip instead of causing the crack to propagate. This leads to larger acoustic emission (AE) occurrences and the release of more substantial energy since more energy is required for fracture development.

The mechanical characteristics of the beddings are crucial in determining the shear displacement between two consecutive acoustic emission (AE) occurrences. More specifically, soft brittle gypsum is less deformable than hard ductile gypsum. This results in a reduced continuity of shear displacement linked to the formation of cracks in the soft layer. This implies that the hard ductile layer and the soft brittle layer, respectively, experience delay failure and fast fracturing. Moreover, the shear strength of a layered model is highly influenced by the mechanical characteristics of the beddings. Soft brittle gypsum has lesser shear strength than hard ductile gypsum, optimizing the shear strength of bedded rock when
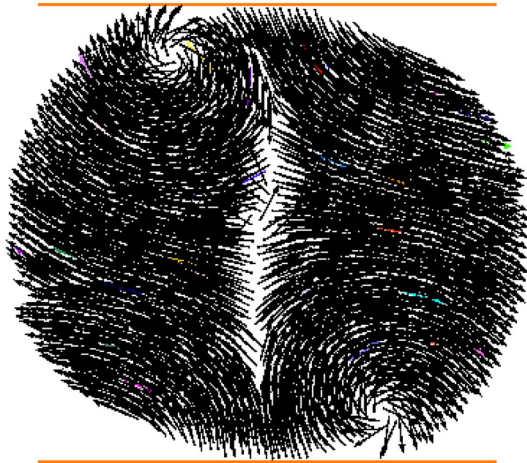
Fig. 16 Typical displacement vector observed in a Brazilian tensile test simulation

hard ductile gypsum occupies a greater fraction of the shear surfaces.

6 Conclusion

This investigation explores the shear mechanism and acoustic emission occurrences within a 2 cm bedding layer under varied normal stress conditions, employing a combination of physical and PFC models. The FJM was used as a practical bond. The following are the primary discoveries of the research:

- In the absence of normal stress, a solitary fracture type was identified, encompassing the initiation of a tensile crack and its propagation perpendicular to the bedding layers. At 2 MPa normal stress, the model exhibited three distinct fracture types: vertical tensile crack propagation in bedding layers, diagonal propagation of mixed-mode shear bands, and breakage of hard rock-soft rock interfaces. The soft layer displayed a higher number of oriented fractures compared to the hard layer, attributed to the brittleness effect of soft material.
- Both of the shear movement associated with peak shear load and shear strength increased with the thickness of hard material in the shearing surface. This suggests that the model containing a soft interlayer demonstrated the highest shear strength and shear movement associated with peak shear load compared to alternative layered models.
- The quantity of major acoustic event hits escalated with the layer number due to the growing number of interfaces. The number of major acoustic evnts in hard material surpassed that in soft material. Both the magnitude of acoustic evnts and the continuity of acoustic evnts rose with normal stress.

- In the brittle model, ultimate failure occurred immediately after crack initiation, while delayed failure was observed in the ductile model.
- shear stiffness, Failure patterns and shear strengths closely mirrored those observed in physical samples. These findings offer valuable insights into the intricate interactions among normal stress, fracture patterns, and acoustic event phenomena within layered rock formations featuring distinct mechanical properties.

Author contributions Seyed Davoud Mohammadi: Supervision, Funding acquisition, Project administration. Rahim Mortezaei: Investigation, Writing-Original draft preparation. Vahab Sarfarazi: Conceptualization, Methodology, Software, Validation, Data curation. Soheil Abharian: Writing- Reviewing and Editing.

Data availability No datasets were generated or analysed during the current study.

Declarations

Conflict of interest The authors assert the absence of any conflicts of interest that are relevant to the content presented in this article.

References

Abharian S, Sarfarazi V, Marji MF, Rasekh H (2022) Experimental and numerical evaluation of the effects of inter-action between multiple small holes and a single notch on the mechanical behavior of artificial gypsum specimens. Theor Appl Fract Mech 121:103462

Aggelis DG, Mpalaskas AC, Ntalakas D, Matikas TE (2012) Effect of wave distortion on acoustic emission characterization of cementitious materials. Construct Build Mater 35:183–190

Aggelis DG, Mpalaskas AC, Matikas TE (2013) Investigation of different fracture modes in cement-based materials by acoustic emission. Cem Concr Res 48:1–8

Cai M, Morioka H, Kaiser PK, Tasaka Y, Kurose H, Minami M, Maejima T (2007) Back-analysis of rock mass strength parameters using AE monitoring data. Int J Rock Mech Min Sci 44(4):538–549

Chang SH, Lee CI (2004) Estimation of cracking and damage mechanisms in rock under triaxial compression by moment tensor analysis of acoustic emission. Int J Rock Mech Min Sci 41:1069–1086

Cheon DS, Jung YB, Park ES, Song WK, Jang HI (2011) Evaluation of damage level for rock slopes using acoustic emission technique with waveguides. Eng Geol 121:75–88

Cho JW, Kim H, Jeon S, Min KB (2012) Deformation and strength anisotropy of Asan gneiss, Boryeong shale, and Yeoncheon schist. Int J Rock Mech Min Sci 50:158–169

Chu WJ, Zhang CS, Hou JA (2013) Particle-based model for studying anisotropic strength and deformation of schist. In: Proceedings of the 3rd ISRM SINOROCK symposium. Shanghai, China, pp 593–96

Dang W, Konietzky H, Frühwirt T (2016) Shear behaviour of a plane joint under dynamic normal load (DNL) conditions. Eng Geol 213:133–141

Donath FA (1961) Experimental study of shear failure in anisotropic rock. Geol Soc Am Bull 72(6):985–989

Duveau G, Shao JF (1998) A modified single plane of weakness theory for the failure of highly stratified rock. Int J Rock Mech Min Sci 35(6):807–813

Duveau G, Shao JF, Henry JP (2015) Assessment of some failure criteria for strongly anisotropic geomaterials. Int J Numer Anal Methods Geomech 3(1):1–26

Esamaldeen A, Wu G, Zhao Z, Jiang W (2014) Assessments of strength anisotropy and deformation behavior of banded amphibolite rocks. Geotech Geol Eng 32:429–438

Gholami R, Rasouli V (2014) Mechanical and elastic properties of transversely isotropic slate. Rock Mech Rock Eng 47:1763–1773

Griffith AA (1921) The phenomenon of rupture and flow in solids. Philos Trans R Soc A 221:163–197

Hakala M, Kuula H, Hudson JA (2007) Estimating the transversely isotropic elastic intact rock properties for in situ stress measurement data reduction: a case study of the Olkiluoto mica gneiss, Finland. Int J Rock Mech Min Sci 44:14–46

Hoek E, Brown ET (1980) Empirical strength criterion for rock masses. J Geotechn Geoenviron Eng 106(9):44–55

Hu X, Su G, Chen G (2019) Experiment on rockburst process of borehole and its acoustic emission characteristics. Rock Mech Rock Eng 52:783–802

Jaeger JC (1960) Shear failure of transversely isotropic rock. Geol Mag 97:65–72

Katsaga T, Sherwood EG, Collins MP, Young RP (2007) Acoustic emission imaging of shear failure in large reinforced concrete structures. Int J Fract 148:29–45

Li BQ, Einstein HH (2017) Comparison of visual and acoustic emission observations in a four point bending experiment on barre granite. Rock Mech Rock Eng 50(9):2277–2296

Li K, Cheng Y, Fan X (2018) Roles of model size and particle size distribution on macro-mechanical properties of Lac du bonnet granite using flat-joint model. Comput Geotech 103:43–60

Liu JP, Li YH, Xu SD, Xu S, Jin CY (2015) Cracking mechanisms in granite rocks subjected to uniaxial compression by moment tensor analysis of acoustic emission. Theor Appl Fract Mech 75:151–159

Lockner D (1993) The role of acoustic emission in the study of rock fracture. Int J Rock Mech Min Sci Geomech Abstr 30(7):883–899

Masri M, Sibai M, Shao JF (2014) Experimental investigation of the effect of temperature on the mechanical behaviour of Tournemire shale. Int J Rock Mech Min Sci 70:185–191

Meglis IL, Chows TM, Young RP (1995) Progressive microcrack development in tests in Lac du Bonnet granite—I. Acoustic emission source location and velocity measurements. Int J Rock Mech Min Sci Geomech Abstr 32(8):741–750

Moradian ZA, Ballivy G, Rivard P (2010) Gravel C, Rousseau B. Evaluating damage during shear tests of rock joints using acoustic emissions. Int J Rock Mech Min Sci 47:590–598

Mortezaei R (2024) Study of shear behavior of non-persistent open joints in heterogeneous and anisotropic rock masses by using rock-like and numerical models. Ph.D. Dissertation, Faculty of Science, Bu-Ali Sina University, Hamedan, Iran

Nasseri MH, Rao KS, Ramamurthy T (1997) Failure mechanism in schistose rocks. Int J Rock Mech Min Sci 34(3–4):219–231

Nasseri MH, Rao KS, Ramamurthy T (2003) Anisotropic strength and deformational behavior of Himalayan schists. Int J Rock Mech Min Sci 40:3–23

Niandou H, Shao JF, Henry JP (1997) Laboratory investigation of the mechanical behaviour of Tournemire shale. Int J Rock Mech Min Sci 34(1):3–16

Ohno K, Ohtsu M (2010) Crack classification in concrete based on acoustic emission. Construct Build Mater 24:2339–2346

Ohtsu M (2010) Recommendation of RILEM TC 212-ACD: acoustic emission and related NDE techniques for crack detection and damage evaluation in concrete. Mater Struct 43:1187–1189

Park B, Min KB (2012) Discrete element modeling of shale as a transversely isotropic rock. In: Proceedings of 7th Asian rock mechanics symposium, Seoul, Korea, pp 336–342

Park B, Min KB (2013) Discrete element modeling of transversely isotropic rock. In: Proceedings of 47th US rock mechanics symposium, San Francisco, US, Paper ARMA13–490

Park B, Min KB (2015) Bonded-particle discrete element modeling of mechanical behavior of transversely isotropic rock. Int J Rock Mech Min Sci 76:243–255

Park S, Hwang C, Choi H Son Y (2021) Application of the punch shear test to evaluate adfreezing strength of frozen soil-structure interface. In: The 2021 world congress on advances in structural engineering and mechanics (ASEM21) GECE, Seoul, Korea, August 23–26, 2021

Potyondy DO (2017) Simulating perforation damage with a flat-jointed bonded-particle material. In: Paper presented at the 51st US rock mechanics/geomechanics symposium, San Francisco, California, USA

Ren F, Liu H, He R, Li G, Liu Y (2018) Point load test of halfcylinder core using the numerical model and laboratory tests: size suggestion and correlation with cylinder core. Adv Civ Eng 7:1–11

Shi XC, Yang X, Meng XF (2016) An anisotropic strength model for layered rocks considering planes of weakness. Rock Mech Rock Eng 49:3783–3792

Shi Z, Li J, Wang J (2022) Effect of the upper limit stress on the fatigue properties and crack propagation processes of sandstones containing pre-existing crack under fatigue-creep interaction. Fatigue Fract Eng Mater Struct 45(5):1391–1405

Singh M, Samadhiya NK, Kumar A (2015) A nonlinear criterion for triaxial strength of inherently anisotropic rocks. Rock Mech Rock Eng 48:1387–1405

Tham LG, Liu H, Tang CA, Lee P, Tsui Y (2005) tension failure of 2-D rock specimens and associated acoustic emission. Rock Mech Rock Eng 38:1–19

Tien YM, Kuo MC (2001) A failure criterion for transversely isotropic rocks. Int J Rock Mech Min Sci 38:399–412

Tien YM, Tsao PF (2000) Preparation and mechanical properties of artificial transversely isotropic rock. Int J Rock Mech Min Sci 37:1001–1012

Tien YM, Kuo MC, Juang CH (2006) An experimental investigation of the failure mechanism of simulated transversely isotropic rocks. Int J Rock Mech Min Sci 43:1163–1181

Tsuyoshi I, Tadashi K, Yuji K (2010) Source distribution of acoustic emissions during an in- situ direct shear test:implications for an analog model of seismogenic faulting in an inhomogeneous rock mass. Eng Geol 110(4):66–76

Wang T, Xu D, Elsworth D (2016a) Distinct element modeling of strength variation in jointed rockmasses under uniaxial compression. Geomech Geophys Geo-Energy Geo-Resour 2:11–24

Wang HJ, Liu DA, Cui ZD, Cheng C, Jian Z (2016b) Investigation of the fracture modes of red sandstone using XFEM and acoustic emissions. Theor Appl Fract Mech 85:283–293

Wang X, Wei Y, Jiang T, Hao F, Xu H (2024) Elastic–plastic criterion solution of deep roadway surrounding rock based on intermediate principal stress and Drucker-Prager criterion. Energy Sci Eng 32:1–21

Wasantha PLP, Ranjith PG, Shao SS (2014) Energy monitoring and analysis during deformation of bedded-sandstone: use of acoustic emission. Ultrasonics 54:217–226

Wasantha PLP, Ranjith PG, Zhang QB, Xu T (2015) Do joint geometrical properties influence the fracturing behaviour of jointed rock? An investigation through joint orientation. Geomech Geophys Geo-Energy Geo-Resour 1(2):3–14

Wu S, Xu X (2015) A study of three intrinsic problems of the classic discrete element method using flat-joint model. Rock Mech Rock Eng 49:1813–1830

Xiao CF, Qiu XD (1983) Investigation of strength and deformation of composite rock in uniaxial and triaxial compression test. J Chongqing Univ 3:23–39

Xiong LX, Chen HJ, Li TB, Zhang Y (2018) Experimental study on the uniaxial compressive strength of artificial jointed rock mass specimen after high temperatures. Geomech Geophys Geo-Energy Geo-Resour 4:201–213

Xiong LX, Xu ZY, Li TB, Zhang Y (2019) Bonded-particle discrete element modeling of mechanical behaviors of interlayered rock mass under loading and unloading conditions. Geomech Geophys Geo-Energy Geo-Resour 5:1–16

Yang SQ, Jing HW, Wang SY (2012) Experimental investigation on the strength, deformability, failure behavior and acoustic emission locations of red sandstone under triaxial compression. Rock Mech Rock Eng 45:583–606

Yang SQ, Yin PF, Huang YH (2019a) Experiment and discrete element modelling on strength, deformation and failure behaviour of shale under Brazilian compression. Rock Mech Rock Eng 52:4339–4359

Yang SQ, Yin PF, Huang YH, Cheng L (2019b) Strength, deformability and X-ray micro-CT observations of transversely isotropic composite rock under different confining pressures. Eng Fract Mech 65(6):77–89

Yang SQ, Yin PF, Ranjith PG (2020) Experimental study on mechanical behavior and brittleness characteristics of longmaxi formation shale in changning, sichuan basin, china. Rock Mech Rock Eng 53:2461–2483

Yin PF, Yang SQ (2018) Experimental investigation of the strength and failure behavior of layered sandstone under uniaxial compression and Brazilian testing. Acta Geophys 66(4):1–21

Yin PF, Yang SQ (2019) Discrete element modeling of strength and failure behavior of transversely isotropic rock under uniaxial compression. J Geol Soc India 93(2):235–246

Zang GM, Li YP, Yang CL (2012) Physical simulation of deformation and failure mechanism of soft and hard interbedded salt rocks. Chin J Rock Mech Eng 31(9):1814–1820

Zhang GM, Li YP, Shi XL (2011) Research on a model material preparation method for alternate layered rock mass and preliminary experiment. Rock and Soil Mech 32:284–289

Zhang H, Elsworth D, Wan Z (2018) Failure response of composite rock-coal samples. Geomech Geophys Geo-Energy Geo-Resour 4(2):175–192

Zhao XG, Cai M, Wang J, Ma LK (2013) Damage stress and acoustic emission characteristics of the Beishan granite. Int J Rock Mech Min Sci 64:258–269

Zhu T, Li Y (2021) Impacts of disk rock sample geometric dimensions on shear fracture behavior in a punch shear test. Comput Model Eng Sci 126(2):455–475